JAGIELLONIAN UNIVERSITY

THE FACULTY OF PHYSICS, ASTRONOMY
AND APPLIED COMPUTER SCIENCE
MARIAN SMOLUCHOWSKI INSTITUTE OF PHYSICS

Hit-time and hit-position reconstruction of gamma quanta in the J-PET tomography system based on a library of model signals

Neha Gupta Sharma

PhD dissertation performed in the Department of Experimental Particle Physics and Applications of the Jagiellonian University
Thesis supervisor : **Prof. dr hab. Paweł Moskal**
Thesis co-supervisor : **Dr Michał Silarski**

Cracow 2017

Contents

1 Introduction **1**

2 Detection Technology **4**
2.1 Interaction of gamma quanta with matter . . . 4
2.1.1 Photoelectric effect . . . 5
2.1.2 Compton scattering . . . 6
2.1.3 Pair production . . . 6
2.2 Scintillation process . . . 7
2.2.0.1 Inorganic scintillator . . . 7
2.2.0.2 Organic scintillator . . . 8
2.3 Intrinsic energy resolution of scintillation detector . . . 9
2.4 Light detection with photomultipliers . . . 10
2.5 Reconstruction of the Line of Response . . . 11

3 Comparison between currently used scanners and the J-PET prototype **13**
3.1 Current PET tomographs . . . 13
3.1.1 Design and physics behind PET . . . 13
3.1.2 Time of Flight PET . . . 14
3.2 Study of cost effective PET . . . 15
3.2.1 Axial geometry . . . 15
3.2.2 The Lead-Walled Straw PET detector . . . 15
3.2.3 The Resistive Plate Chamber PET detector . . . 16
3.3 The J-PET Prototype . . . 17
3.3.1 Design and physics behind J-PET . . . 17

4 The two strip J-PET prototype **21**
4.1 Experimental setup . . . 21
4.1.1 Format of collected data . . . 22
4.2 Correction and selection of data . . . 23
4.2.1 Pedestal correction . . . 23
4.2.2 Data Selection . . . 24

5 Hit-position and hit-time reconstruction method based on library of model signals **27**
5.1 Working principle of hit-position and hit-time reconstruction method . . . 27

5.2 Distance metrics . . . 29
5.2.1 Chi-square test . . . 30
5.2.2 Mahalanobis metric . . . 30
5.3 Reconstruction method . . . 30
5.3.1 Library of synchronized model events . . . 31
5.3.1.1 Synchronization of signals . . . 31
5.3.1.2 Determination of model events shape . . . 32
5.3.2 Reconstruction of hit-position and hit-time . . . 34
5.3.2.1 x - vector . . . 34
5.3.2.2 Covariance Matrix . . . 35
5.3.2.3 Hit-position . . . 36
5.3.2.4 Hit-time and Time-of-flight . . . 37

6 Optimization of signals processing 39
6.1 Optimization of signals processing from two strips module with dimension of 5x19x300 mm^3 strips . . . 39
6.1.1 Optimization of constant-level discriminator . . . 39
6.1.1.1 Single-threshold level . . . 40
6.1.1.2 Two-threshold level . . . 40
6.1.1.3 Three-threshold level . . . 43
6.1.2 Optimization of energy deposition . . . 44
6.1.2.1 Bisection of energy region . . . 44
6.1.2.2 Multisection of energy region into four parts . . . 45
6.1.3 Optimization of number of parameters in Mahalanobis distance . . 46
6.2 Optimization of signals processing from two strips module with dimensions 7x19x500 mm^3 . . . 48
6.2.1 Optimized two-threshold level . . . 48
6.2.2 Optimized energy distribution . . . 48
6.3 Multi-threshold Technique . . . 49

7 2D Image reconstruction 52
7.1 Spatial resolution . . . 53

8 Results 54
8.1 J-PET prototype of two 5x19x300 mm^3 strips . . . 54
8.1.0.1 Spatial resolution . . . 58
8.2 J-PET prototype of two 7x19x500 mm^3 strips . . . 60

9 Summary and perspectives 65

Wydzial Fizyki, Astronomii i Informatyki Stosowanej
Uniwersytet Jagielloński

Oświadczenie

Ja niżej podpisana mgr Neha Gupta-Sharma (nr indeksu: 1105647) doktorantka Wydziału Fizyki, Astronomii i Informatyki Stosowanej Uniwersytetu Jagiellońskiego oświadczam, że przedłożona przeze mnie rozprawa doktorska pt. "Hit-time and hit- position reconstruction of gamma quanta in the J-PET tomography system based on a library of model signals" jest oryginalna i przedstawia wyniki badań wykonanych przeze mnie osobiście, pod kierunkiem prof. dr hab. Pawła Moskala. Pracę napisałam samodzielnie.

Oświadczam, że moja rozprawa doktorska została opracowana zgodnie z Ustawą o prawie autorskim i prawach pokrewnych z dnia 4 lutego 1994 r. (Dziennik Ustaw 1994 nr 24 poz. 83 wraz z późniejszymi zmianami).

Jestem świadoma, że niezgodność niniejszego oświadczenia z prawdą ujawniona w dowolnym czasie, niezależnie od skutków prawnych wynikających z ww. ustawy, może spowodować unieważnienie stopnia nabytego na podstawie tej rozprawy.

Kraków, dnia..... .....
podpis doktorantki/doktoranta

Abstract

Positron Emission Tomography (PET) is an advanced nuclear medicine imaging modality. It enables to determine the diseases (like cancer, heart diseases etc) in vivo in their earliest stage which significantly influence the health-care resources provided to the patient. However, high cost of PET scanners construction has limited their availability.

J-PET (Jagiellonian-PET) is one of the project started with the aim to build a more economical PET modality. It is an assemble of plastic scintillators in a cylindrical fashion with large longitudinal field-of-view (FOV). In the plastic scintillators gamma quanta emitted from the patient's body interact via Compton scattering. Therefore, amplitudes of processed signals strongly depend not only on the hit-position but also on the energy deposition which demands for a new reconstruction method.

The aim of this work is to develop a new reconstruction method for hit-time and hit-position of the registered gamma quanta. The developed method is based on the evaluation of degree of similarity between the registered signals and model signals stored in a database. The compared signals are expressed in the form of an array including times determined when sampling the signal in voltage domain. As a measure of similarity the Mahalanobis distance between the examined and model signals is used. The *model signal* is referred to as a signal which shape is determined from the measured experimental data. The hit-position and hit-time are defined as the time and position of the model signal at most similar to the registered one. The method is optimized for number of threshold levels with different combinations, energy loss regions and number of parameters included to calculate the value of Mahalanobis distance. Time-of-flight resolution is used as a criterion of optimization. The final conclusion is that the reconstruction of image will be performed on the two-threshold levels followed by the bisection of energy region from 0.2 MeV to 0.38 MeV in two parts using Mahalanobis distance as a function of position (z) and time shift (Δt).

The method was validated on the J-PET two-strips prototype, for two sets of strips modules: one with dimensions 5x19x300 mm^3 and the second with dimensions 7x19x500 mm^3. As a result the obtained time-of-flight resolutions for the annihilation point in the center of the detector are equal to 325 ps (FWHM) and 414 ps (FWHM) for the modules with dimensions of 5x19x300 mm^3 and 7x19x500 mm^3, respectively. Spatial resolutions when gamma was hitting at the center of the scintillator for module with dimensions 5x19x300 mm^3 and 7x19x500 mm^3 are equal to 25.2 mm (FWHM) and 32.3 mm (FWHM), respectively. Spatial transverse and axial resolutions obtained from the image reconstructed by the J-PET two-strips prototype for point-like source placed at the center of the detector with maximum likelihood expectation maximization algorithm using two-strip module with dimension 5x19x300 mm^3 are equal to FWHM = 7.7 mm and FWHM = 20.2 mm, respectively.

Results obtained in this thesis constitute a basis for the construction of the J-PET full frame prototype built out of 192 scintillators arranged in cylindrical geometry in 3 layers with inner diameter of 85 cm and axial length of 50 cm.

Streszczenie

Pozytonowa Tomografia Emisyjna (PET) jest jedną z najbardziej zaawansowanych metod obrazowania medycznego. Pozwala ona na wykrycie zmian chorobowych (nowotworów, chorób serca itp.) in vivo, w ich pocztkowym stadium, co znacząco wpływa nowotworów na planowanie terapii oraz strategię leczenia. Niestety wysokie koszty budowy oraz zakupu skanerów PET ograniczają ich dostępność.

J-PET (Jagiellonian-PET) jest jednym z projektów badawczych mających na celu budowę bardziej ekonomicznego skanera PET. Tomograf J-PET zbudowany jest z długich scyntylatorów plastikowych tworzących cylindryczny detektor z dużym polem obrazowania (FOV). Kwanty gamma emitowane z ciała pacjenta oddziałują ze scyntylatorami plastikowymi głównie poprzez efekt Comptona, dlatego amplitudy sygnałów cząstek rejestrowanych przez te detektory zależą nie tylko od deponowaej energii, ale również od miejsca reakcji kwantu gamma w detektorze. Dlatego potrzebna jest nowa metoda rekonstrukcji miejsca oraz czasu reakcji kwantu gamma z materiałem detektora.

Celem tej pracy jest stworzenie nowej metody rekonstrukcji pozycji oraz czasu reakcji kwantów gamma w długich detektorach scyntylacyjnych. Zaproponowana metoda oparta jest na określeniu stopnia podobieństwa pomiędzy rejestrowanym sygnałem oraz sygnałem modelowym ze stworzonej wcześniej bazy danych. Porównywane sygnał przedstawione są jako wektor czasów otrzymanych przez próbkowanie w domenie napięcia. Jako miarę podobieństwa sygnałów wykorzystano odległość Mahalanobisa, a miejsce oraz czas reakcji kwantów gamma określane jest jako pozycja oraz czas sygnału modelowego najbardziej podobnego do rejestrowanego. Metoda została zoptymalizowana pod kątem liczby oraz wartości napięć na jakich próbkowany jest sygnał, deponowanej energii oraz liczby parametrów wykorzystywanych w określaniu odległości Mahalanobisa, a jako kryterium optymalizacji wykorzystana została rozdzielczość czasu przelotu mierzonego pomiędzy dwoma modułami prototypu tomografu. W wyniku przeprowadzonych badań optymalne okazało się wykorzystanie w rekonstrukcji obrazu tomograficznego dwóch progów próbkowania sygnałów, podziału zakresu deponowanej energii od 0.2 MeV do 0.38 MeV na dwa zbiory oraz określanie odległości Mahalanobisa w funcji pozycji (z) oraz czasu (Δt).

Zaproponowana metoda został przetestowana na dwu-modułowych prototypach tomografu J-PET zbudowanych z pasków scyntylacyjnych o wymiarach 5x19x300 mm^3 oraz 7x19x500 mm^3. Otrzymane dla tych prototypów rozdzielczości czasu przelotu dla źródła kwantów anihilacyjnych umieszczonego w środku geometrycznym układu detekcyjnego wyniosły odpowiednio 325 ps (FWHM) oraz 414 ps (FWHM). Ponadto, rozdzielczości przestrzenne rekostruowanego punktu reakcji kwantów gamma dla tych prototypów wyniosły odpowiednio 25.2 mm (FWHM) oraz 32.3 mm (FWHM). Rozdzielczości w kierunkach transwersalnym oraz aksjalnym obrazu otrzymanego dla punktowego źródła kwantów anihilacyjnych umieszczonego w środku geometrycznym prototypu o wymiarach 5x19x300 mm^3 i zrekonstruowanego z wykorzystaniem algorytmu maksymalnej wiarygodności wynoszą odpowiednio FWHM = 7.7 mm oraz FWHM = 20.2 mm.

Otrzymane wyniki zostały wykorzystane w projekcie i budowie pełnego prototypu tomografu J-PET składającego się ze 192 modułów scyntylacyjnych, które tworzą 3 warstwy detekcyjne o wewnętrznej średnicy 85 cm oraz długości około 50 cm.

Chapter 1

Introduction

Positron Emission Tomography (PET) is one of the most advanced nuclear medicine imaging techniques that have potential to identify diseases (like cancers, heart disease, gastrointestinal, endocrine, neurological disorders and other abnormalities) in vivo in its earliest stage which can effectively improve the health-care delivery resources to the patient. PET uses a β^+ radioactive tracer which is injected into the patient's body. This radioactive tracer eventually is accumulated in the organ or area of the body being examined and emits pairs of back-to-back 511 keV gamma quanta in coincidence. These gamma photons are produced by the annihilation of a positron emitted by the radio-tracer with an electron present in the patient's body.

At present all commercial PET scanners use block of inorganic crystal scintillators as the gamma radiation detectors [1, 2]. These block detectors are arranged in a ring with a diameter of 70-100 cm [1, 2]. Current PET scanners offer an axial extent of 17-25 cm allowing to scan only a small part of patients body at a time. In order to examine the large part of the body at the same time it requires bigger number of detectors which increase significantly the cost of scanner's construction.

Time resolution obtained by current best PET scanners is about 316-400 ps [1] which corresponds to the spatial resolution of 4.7-6 cm along the line-of-response (LOR). Presently, research aiming to improve the performance of current PET scanners is ongoing including:

- reduction of noise for the effective application of the 3D image reconstruction,
- reconstruction of depth of interaction of gamma quanta in the thick detector material,
- building a large diagnostic chamber in a cost effective way.

One possible solution to realize the mentioned requirements is the use of polymer scintillator which are much cheaper than crystals [3]. Typically, price per unit of volume for polymer scintillators is more than a factor of 50 lower than the crystal. In addition, they can be produced easily in various sizes and shapes. The light attenuation length of plastic scintillator is very large, typically $\sim$2 m [4–6] and it is about 10 times larger with respect to the crystals [7]. Moreover, plastic scintillators possess relatively low refractive index of about 1.5 [6] in comparison to $\sim$1.8 of inorganic crystals [6]. This property for long

path length implies smaller time spread and hence, better time resolution. Additionally, plastic scintillators have a very short decay time in comparison to crystals. This also results in better time resolution. Furthermore, using axially arranged plastic scintillators it is possible to build a diagnostic chamber with more than one detection layer which will increase the sensitivity [8]. The improvement of the image quality is also expected due to the improved time resolution [9]. In order to achieve a goal of more economical PET scanner with large acceptance and improved time resolution, a new project to build a TOF-PET (Time−of−flight PET) detector using polymer scintillators [3, 10–12] has started in Jagiellonian University, Krakow (research and development stage). This thesis is a part of this project. Its larger longitudinal field-of-view allows to scan a larger part of patient's body at a time in contrast to currently used PET scanners. In the J-PET (Jagiellonian-PET) scanner, amplitude of signals used for reconstruction strongly depends both on the hit-position and on energy deposited by gamma quanta. Therefore, a new hit-position reconstruction method is required [13–16]. In present work, such method of hit-position and TOF reconstruction is developed. It is based on the determination of degree of similarity between registered and synchronized model signals stored in a database. Mahalanobis distance [17] is used as a measure of similarity between the two compared signals [18, 19]. It is a measure of deviation of the mean values of different variables in multivariate analysis. The deviation is calculated with the consideration of correlation between the variables. In general this reconstruction method can be used in other PET modalities in which signals are sampled in voltage domain by means of multi-threshold constant-level discriminators or constant fraction discriminators. It has been validated on the experimental data measured with two strips J-PET module, where a Serial Data Analyzer (SDA) was used to sample the signals with a time interval of 100 ps. However, in a full-scale J-PET tomograph signals will be sampled by a dedicated front-end electronics (FEE) in voltage domain which offers the time resolution of about 20 ps [20].

Two-strip module was the first J-PET prototype built to use the plastic scintillator as a radiation detector despite of its low density and small atomic number. Since the study is itself a challenge so, it is very necessary to monitor the performance of plastic scintillator at each step of experiment in order to have the maximum output from it. This demands a series of experiments which include: selection of efficient polymer scintillator (shape and dimensions), search for the best specular reflecting foil, study of scintillator strips with different orientation (axially or radially), testing and calibration of photomultiplier tubes etc. So, the work was not only limited to the development of reconstruction method but also contributed significantly in the aforementioned experiments and their analyses. Conclusions drawn from these experiments were implemented in the two-strip J-PET module explained in this work.

Thesis has been organized in the following way: Chapter 2 emphasizes on the theoretical background of the detections techniques e.g. interaction of gamma quantum in matter, scintillation processes, light conversion to the electrical signals with photomultiplier. In Chapter 3 current modalities and newly developed J-PET concept is described. In Chapter 4 the detailed description of experimental setup, collection and filtration of data is given. The idea of the presented method (within confines of this work) and the detailed explanation of the mathematical basis of the proposed algorithm is presented in Chapter 5. In Chapter 6 optimization of different parameters has explained. Brief descrip-

tion of image reconstruction method is presented in Chapter 7. The experimental results are given in Chapter 8. Finally, the results are discussed and summarized in Chapter 9.

Chapter 2

Detection Technology

One of the most important component of any imaging modality is its detection system. The PET imaging technology is based on the annihilation process of an emitted positron and an electron. As the result of annihilation, a pair of almost back-to-back gamma-photons (having energy of 511 keV each) are emitted. These two anti-collinear high energy photons are detected by the pair of detectors which allow to identify the line-of-response (LOR) including the annihilation point. By acquiring a large number of LORs (several millions), it is possible to reconstruct the distribution of the radioactive nuclei inside the volume studied using an appropriate algorithm. The method is pictorially depicted in Fig.2.1. In this chapter detection technologies used in commercial PET and J-PET are reported in detailed.

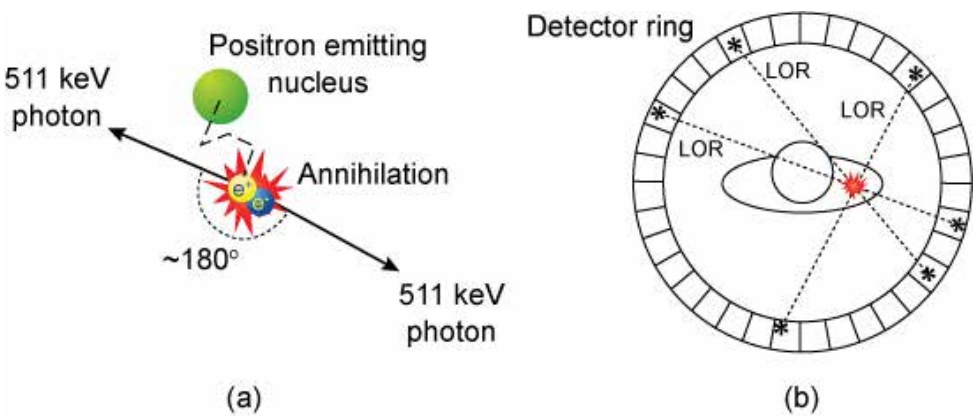

Figure 2.1: Basic principle of the PET tomography. The figure is adapted from [21]

2.1 Interaction of gamma quanta with matter

There are three main modes of interactions by which gamma quanta interacts with matter: photoelectric effect, Compton scattering and pair production. Fig.2.2 shows the relative importance of these three phenomena as a function of photon energy and material's atomic number.

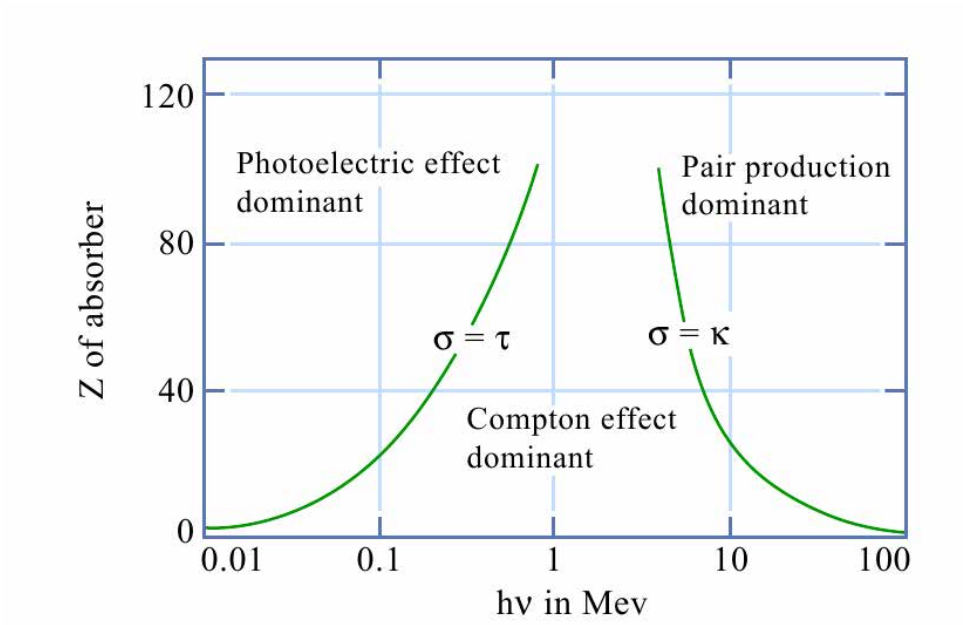

Figure 2.2: Dominant modes of γ interaction as a function of its energy and material's atomic number [22], where, τ and κ are the linear attenuation coefficients of photoelectric and pair-production, respectively.

2.1.1 Photoelectric effect

In the photoelectric effect, the incident photon is absorbed by the atom, and as a result an electron is ejected from one of its inner shells (see Fig.2.3). Eq.2.1 shows the relation between energy of incident gamma E_γ, kinetic energy E_e and binding energy E_{BE} of an ejected electron [23].

$$E_e = E_\gamma - E_{BE} \tag{2.1}$$

The vacancy created by the electron is filled by the electron of outer orbital followed by emission of characteristics x-ray or an Auger electron. This effect dominates for low energy-range gamma (upto several hundreds of keV).

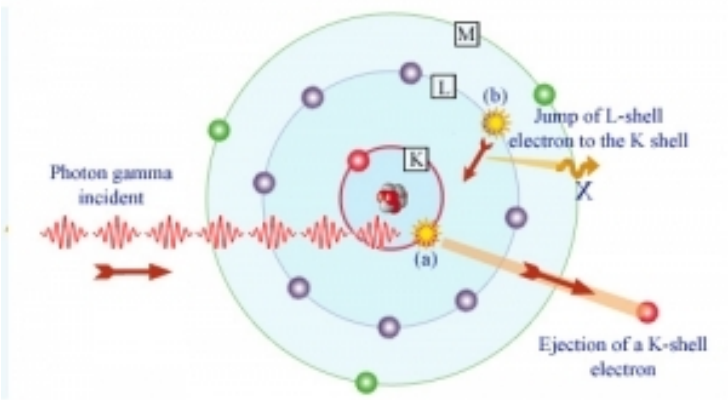

Figure 2.3: The photoelectric effect. The figure is adapted from [24]

2.1.2 Compton scattering

The Compton effect means an inelastic scattering of gamma quanta by a free or loosely bound (quasi-free) electron (see Fig.2.4). The amount of energy transferred to the electron equals to the difference between the energies of incident and scattered photon. The occurrence of Compton scattering is most probable over the range of energies between few keV to MeV.

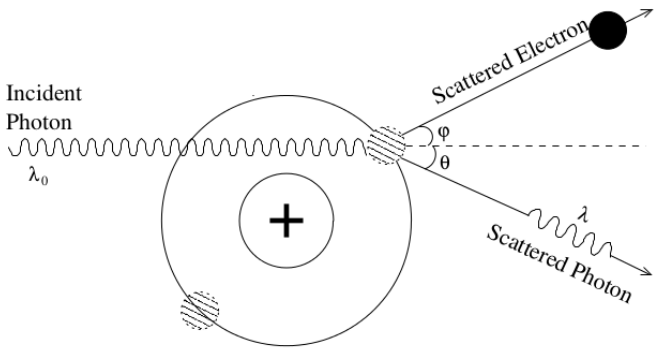

Figure 2.4: The Compton Effect. The figure is adapted from [25].

The Compton scattering probability on a single electron decreases with increasing energy of gamma ray and is almost independent from atomic number (Z). Momentum and energy conservation laws lead to Eq.2.2 for energy of scattered electrons [23]:

$$E_{\gamma}^{'} = \frac{E_{\gamma}}{1 + \frac{E_{\gamma}}{E_0}(1 - \cos\theta)} \tag{2.2}$$

where E_{γ}, $E_{\gamma}^{'}$ are the energies of incoming and scattered photons, respectively and θ is the scattering angle. $E_0 = 0.511$ MeV is the rest mass energy of the electron. In the PET tomography E_{γ} has the same value as E_0 so the above equation reduces to :

$$E_{\gamma}^{'} = \frac{511}{2 - \cos\theta} \qquad [\text{keV}] \tag{2.3}$$

In the J-PET modality Compton scattering plays an important role.

2.1.3 Pair production

This process (see Fig.2.5) can only occur when energy of incident gamma is greater than 1.02 MeV. Photons with such energy get absorbed in the vicinity of nucleus and produce a positron-electron pair leaving behind the atom in an excited state. From energy conservation law, energy of photon responsible for pair-production process should be greater than the sum of a positron and an electron's rest mass. Gamma photons produced in PET have too low energy (511 keV) for this process to occur.

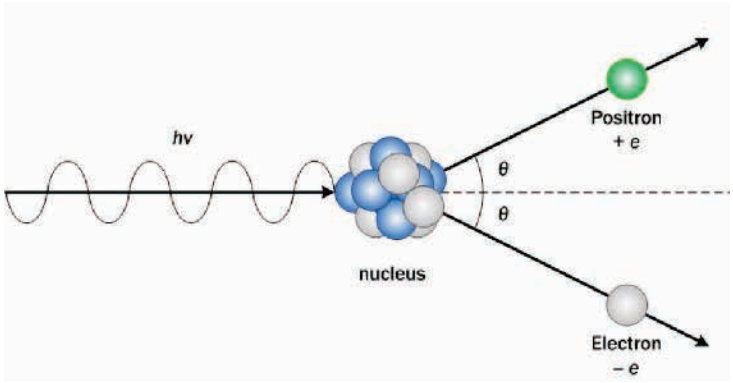

Figure 2.5: Pair production. The figure is adapted from [26].

2.2 Scintillation process

PET scanners use scintillating material which absorb the incident gamma-ray and converts its energy into a pulse of visible (or ultraviolet (UV)) photons which is called scintillation process. According to [27] the overall efficiency η of the conversion process may be characterized as a product of 3 factors:

$$\eta = \beta SQ \tag{2.4}$$

where β is the conversion efficiency of the gamma-ray energy to electron-hole pairs, S is the transfer efficiency of the energy held by the electron-hole pairs to the activator ions or other luminescence centers and Q is the quantum efficiency of the luminescence centers themselves. Based on these factors scintillators are characterized with 3 parameters: light output, decay time and energy resolution.

In commercial PET scanners the material used to detect the annihilation gamma quanta is an inorganic scintillator. However, in the newly developed PET scanner by J-PET collaboration organic scintillators are used as a radiation detectors.

2.2.0.1 Inorganic scintillator

In nuclear medicine field crystalline inorganic scintillators play an important role. In such scintillators, scintillation mechanism depends on the electron-hole pairs created in valence and conduction band when they come in contact with the radiation. In pure crystal the energy gap between valence and conduction band is very large. As a result the photons are emitted with energy higher than the visible range of electromagnetic spectrum. In order to force the emitted photon to lie in the visible range of electromagnetic spectrum small amount of impurities called activators are added. The activator modifies the energy band structure of the crystal. The activator creates the luminescence centers in the forbidden energy region of pure crystal which helps electrons to de-excite with the emission of photons in visible range of electromagnetic spectrum [23]. This is illustrated in Fig. 2.6.

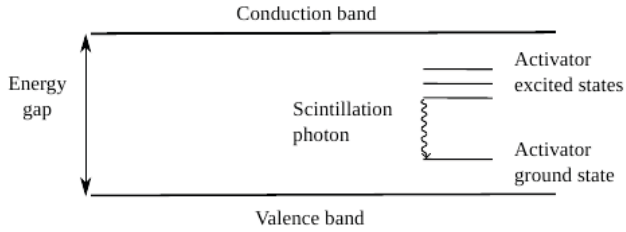

Figure 2.6: Energy band structure of an activated crystal scintillator [23].

2.2.0.2 Organic scintillator

Organic scintillators are the compounds of aromatic hydrocarbon containing linked or condensed benzene-ring structures which have symmetry properties associated with electron structure known as π-electron structure [28]. Generally, they are classified into three types: crystalline, liquid and plastic. Scintillation light in such scintillators arises from the fluorescence process which follow the transitions between different energy levels of a single molecule [23]. The transition involve absorption of energy and excitation of electron from singlet ground state (S_0) to excited singlet (S_1, S_2, S_3...). or triplet state (T_1, T_2, T_3...) shown in Fig. 2.7. Energy space between the singlet states S_0 and S_1 is of about 3-4 eV whereas the other higher-lying states have smaller spacing between them. There are further sub-division of these levels into more levels called vibrational states. These vibrational levels have a space of about 0.15 eV and represented by S_{00}, S_{01}, T_{10}, T_{11}..). At room temperature thermal energy of a molecule is about 0.025 eV which is very small in comparison to the spacing between the vibrational states. As a result at room temperature, nearly all the molecules stay at S_{00} state (lowest vibrational state of ground state S_0). Higher singlet states de-excited (within picoseconds) to S_1 state through radiationless transitions (internal conversion and the states like S_{11} or S_{12} with excess vibrational energy also de-excited to S_10 state [23]. As a result, S_{10} state becomes most populated within a very short time and started to de-excite through prompt fluorescence (as shown in Fig.2.7). The prompt fluorescence intensity at time t is described by:

$$I = I_0 e^{-\frac{t}{\tau}} \tag{2.5}$$

where τ is the fluorescence decay time for the S_{10} level . In most organic scintillators, τ is of the order of few nanoseconds (leading to small rise and decay time) therefore organic scintillators are fast [23].

Other possibility is the transition through triplet state T_1 (as shown in Fig.2.7). Generally, triplet state T_1 has longer lifetime than the singlet state S_1. Hence, electrons from S_1 state first de-excite to T_1, and then de-excite to S_0 (ground) state. The de-excitation of electron from T_1 to S_0 results in the emission of phosphorescence. The resultant phosphorescence spectrum has longer wavelength in comparison to fluorescence spectrum as T_1 state lies below S_1 state [23].

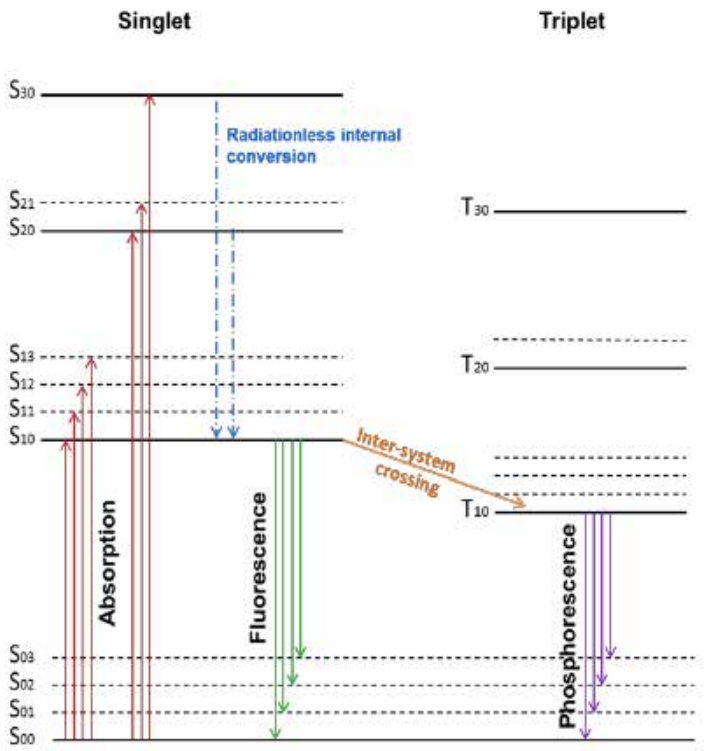

Figure 2.7: Scintillation mechanism in organic scintillator. The figure is adapted from [23].

Plastic scintillators In nuclear and particle physics, plastic forms of organic scintillators are widely in used. Typically they are the ternary system consisting of a base, primary fluor (main organic scintillator) and secondary fluor called wavelength shifter (WLS). The base is a polymerized liquid like styrene or vinyltoluene and emits radiation in UV region, which is not detected by the photomultipliers. In order to detect the emission spectra of base the wavelength was shifted towards the visible region (longer wavelength) using wavelength shifter (see Fig.2.8). Selection of wavelength shifter depends on the desired wavelength of emitted photons [28, 29].

2.3 Intrinsic energy resolution of scintillation detector

The term energy resolution refers to the ability of detector to well distinguish the gamma quanta with energies lying in the close proximity of each other with the limitation imposed by the physical characteristics of the scintillator and readout devices. It is mainly affected by the intrinsic energy resolution of the scintillator materials. Generally the obtained energy spectrum is a Gaussian like peak instead of an ideal delta-function peak because of the fluctuations in number of excitations and ionizations in the detector material. Hence, the energy resolution R is defined as the full width at half maximum (E_{FWHM}) of the energy peak. The relation between energy resolution and standard deviation, σ, of

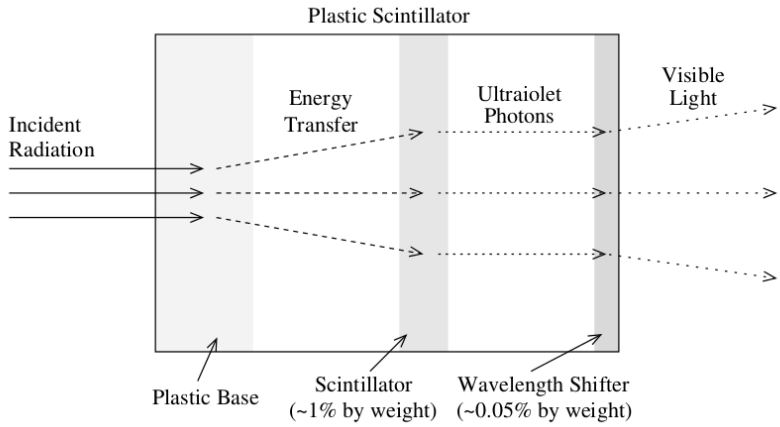

Figure 2.8: Working mechanism of plastic scintillator. Incident radiation interacts with plastic base. Deposited energy is then transfered to the scintillator. The scintillator produced an ultraviolet photons which are shifted to visible light region by the wavelength shifter [25].

the peak is as follows:

$$E_{FWHM} = 2.35\sigma \tag{2.6}$$

The better the energy resolution, the better the signal-to-noise ratio of the reconstructed PET images [30]. Number of photons detected by the photo-detector [31] is the primary limitation on energy resolution of any scintillator. The bigger the number of photons, the better is the energy resolution, as it lowers the statistical fluctuations.

The energy resolution of the whole detection system R, is divided into three parts: intrinsic energy resolution of the scintillator, R_i , transfer resolution, R_p, and the resolution of photomultiplier tube (PMT), R_m [32]. Their contribution to overall energy resolution is shown in Eq.2.7

$$R^2 = {R_i}^2 + {R_p}^2 + {R_m}^2 \tag{2.7}$$

The transfer resolution is generally neglected [33] and the photomultiplier resolution is described by:

$$R_m = 2.35\sqrt{\frac{1 + v(M)}{N_p}} \tag{2.8}$$

where $v(M)$ is the variance of photomultiplier gain and N_p is the number of photoelectrons.

2.4 Light detection with photomultipliers

Photomultipliers have been used for many years to detect low-energy photons in the UV to visible range, high-energy photons (X-rays and gamma rays) and ionizing particles

using scintillators. It is a vacuum tube consisting of a photocathode, focusing electrodes, several dynodes and an anode, as shown in Fig.2.9. Typically 1000 to 2000 volts of high voltage [34], is applied across the tube to keep each dynode at higher potential than the previous one. Incident photon hits the photocathode and knocks out a low-energy electron called photoelectron, from the photoemissive material via photoelectric effect. Then the electric field inside the tube accelerates the photoelectrons and the focusing electrodes guide the photoelectron to the first dynode where re-emission of several secondary electrons occurs. These secondary electrons are then in turn accelerated towards the successive dynodes, where they knock out more electrons. This acceleration and multiplication of electrons is continued to the last dynode where pulse of electrons is formed and attracted to the anode. A typical PMT consists of 10 to 12 dynodes [35] and amplifies the signal with a factor of 10^5 to 10^7 [36]. This factor is known as the gain of the photomultiplier. PMTs exhibit linear amplification of the signal, high gain, good SNR (signal-to-noise ratio), and a short signal pulse [23]. On the other hand, they are quite large and have a relatively low quantum efficiency of about 20% [35]. They are also sensitive to magnetic fields, which limits their usage in magnetic environments.

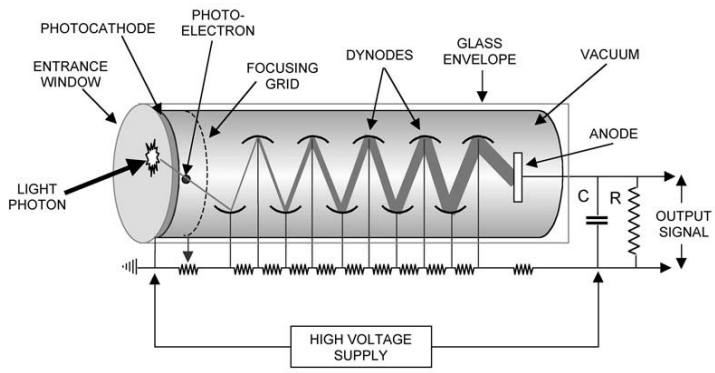

Figure 2.9: Photomultiplier Tube. The figure is adapted from [37]

2.5 Reconstruction of the Line of Response

Majority of articles [38–40] have explained the basics of reconstruction of line of response in PET so, in the following section only a brief description of the method is presented.

As defined earlier in the PET a pair of gamma-rays (having energy of 511 keV) are emitted back-to-back. They are detected by a pair of detectors using coincidence method. In coincidence mode a predefined time window is used. If the detected photons are registered within the defined time window then a line of response between the two respective detectors is constructed. After registration of an event, the next step is to fulfill the criteria of event selection, which includes registration of an event within the defined energy window and acceptance angle. If the registered event fulfilled these two criteria then it is considered as a valid event [35] and used for the image reconstruction. But it is not necessary that the assigned line of response for a valid event pass through the actual point of annihilation. There is a possibility that before detection one or both of the pho-

tons have undergone interactions in which they lost energy or changed direction in the tissue [25]. These kind of processes give rise to different coincidence detection: True , scattered, random and multiple.

- **True coincidence** in which the photons pass through the subject without any interaction and are subsequently detected. They provide the valuable information about the distribution of radioactive-tracer inside the patient.
- **Scattered coincidence** occurs if one or both of the photons changed their direction before detection.
- **Random coincidence** happens when the registered photons come from the different annihilation points. They add an undesirable background to the reconstructed image.
- **Multiple coincidence** takes place when more than two photons are detected within defined time window due to which there are more than one possible LORs.

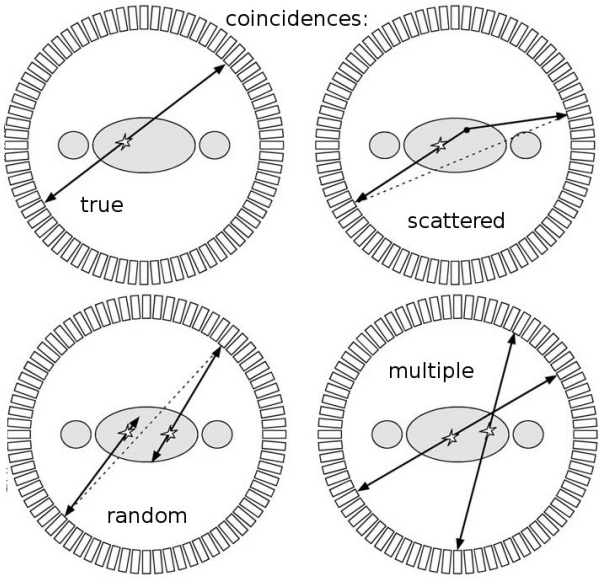

Figure 2.10: Pictorial representation of different types of coincidences to deal with in the PET tomography [37].

Their pictorial representation is shown in Fig.2.10. In multiple events there is no way to determine which photons come from the same annihilation point so they are discarded. Scattered and random coincidences deteriorate the resolution and contrast of final reconstructed image [35] and are thus unwanted.

Chapter 3

Comparison between currently used scanners and the J-PET prototype

3.1 Current PET tomographs

3.1.1 Design and physics behind PET

Commercially used PET scanners are built out from block detectors (inorganic scintillators) arranged in a ring with a typical diameter of 70-100 cm and an axial extent of 17-25 cm [1, 2]. Typically, 3 cm thick single-block detector consists from a crystal partially cut (with the deepest cuts at the edges) into smaller pieces (mostly, 8 x 6 elements) separated from each other with reflective material. Each scintillator block is coupled to four photomultipliers as it is shown in Fig. 3.1. There is a linear distribution of scintillation light between all of the photomultipliers. The amplitude distribution of the signals obtained from the photomultipliers allows to determine the place of interaction of gamma quantum within the crystal with an accuracy equivalent to the size of smallest crystal element. In the current PET scanners coincidence circuitry between each detector pair is not possible as they are grouped together into sets.

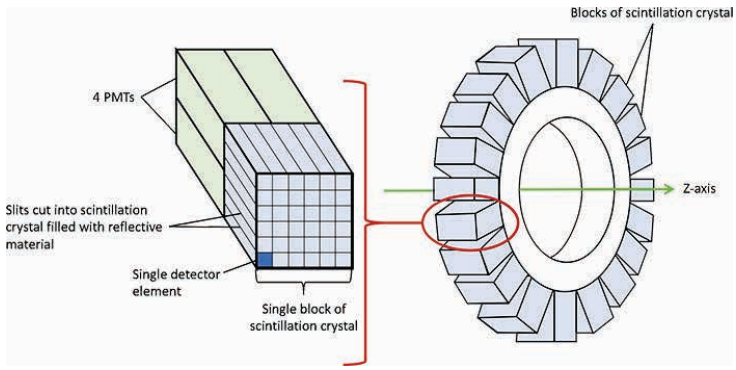

Figure 3.1: A typical commercial block detector (8 x 8) attached to four square PM tubes and the arrangement of such blocks in a ring [41].

Typical spatial resolution obtained in clinical PET images is about 4 mm with the

assumption that the gamma quantum has been absorbed in the middle of the detector element an essential condition limiting the resolution [12]. One of the possible solution to improve the resolution of tomographic image is to use the information of time-of-flight (TOF). The method is explained in the next section.

3.1.2 Time of Flight PET

TOF term in PET can be defined as the difference of arrival time between the two registered annihilation photons. This is not measured in conventional PET. But in TOF-PET this is measured and utilized in order to determine the point of annihilation more accurately. Its principle is explained in Fig.3.2. Using Eq.3.1 one can determine the annihilation point:

$$\Delta s = c\Delta t/2 \tag{3.1}$$

where Δs is the distance from the center of the line of response to the annihilation point, Δt is the time difference of the two photons arrival and c is the speed of light($\sim$ 30 cm/ns). The time-of-flight information helps to reduce the noise along the line of response and hence, improved the quality of obtained tomographic image and time resolution [9, 42, 43]. Philips introduced the first commercial PET scanner in 2005-2006. It is built from LYSO scintillator crystals with time-of-flight information and obtained a coincidence time resolution of about 585 ps [2, 44]. In 2008, SIEMENS achieved a time resolution of about 540 ps with the prototype built from LSO crystals [45, 46]. Meanwhile GE also developed a TOF-PET scanner using LYSO crystals and obtained a time resolution of about 544 ps [2, 46]. In 2009, one more TOF-PET (Vereos) scanner was noticed. It was developed by PHILIPS with improved electronics and new digital SiPM [47]. With this prototype the time resolution of about $\sim$345 ps and spatial resolution of about 5.2 cm along LOR were obtained [2, 46, 47]. Currently, research with aim to construct a cost effective PET scanner with better time properties is ongoing. Few such studies are mentioned in the next section.

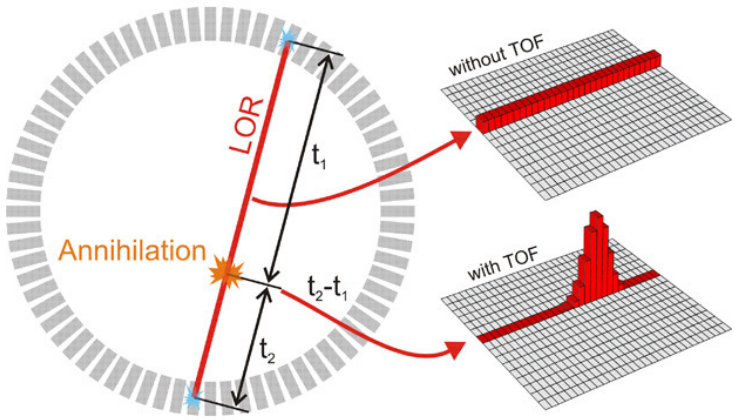

Figure 3.2: Difference between coventional PET and TOF-PET. In case of PET the probability of annihilation along the LOR line is homogeneous, while in TOF-PET only a part of LOR line is taken into account for reconstruction [48].

3.2 Study of cost effective PET

3.2.1 Axial geometry

In all available commercial PET scanners scintillators are arranged radially, but nowadays a new project to built a PET scanner with an axial geometry has been undertaken by many collaborations like CIMA [49] or AX-PET [50]. Geometrical view of novel device developed by both collaborations are shown in Fig.3.3. Axial concept offers higher efficiency because, the detector thickness plays no role in radial direction and gives the possibility to recover a fraction of gamma's undergoing double interactions (first Compton and then photoelectric in a different crystal of the same array) [49]. All these facts help in improving the spatial resolution, sensitivity and efficiency of PET scanners. Both collaborations have used long LYSO crystal scintillators of dimensions 100 x 3 x 3 mm^3 arranged axially and stacked in several layers and achieved competitive performance in terms of energy and spatial resolutions.

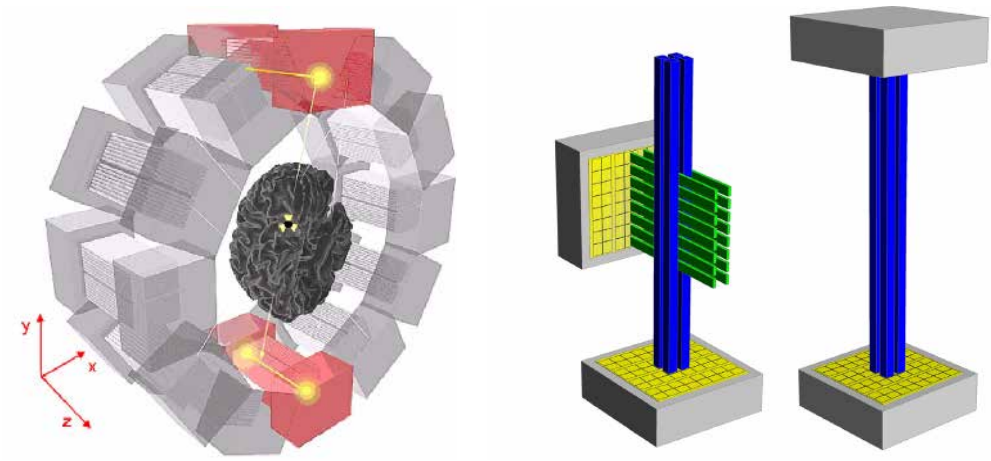

(a) (b)

Figure 3.3: (a) Schematic view of 3D axial HPD-PET developed by the CIMA collaboration [49]. (b) Sketch of single and dual sided AX-PET module consisting of 2 layers of 2 crystals and 8 WLS strips each [50].

3.2.2 The Lead-Walled Straw PET detector

To construct a cost effective PET scanner, a novel wire detector design based on the lead walled straw (LWS) modules has been developed [51, 52]. This technique is an alternative for crystal scintillator to build a PET scanner at low cost. Such detectors can easily be produced in close-packed arrays shown in Fig.3.4 with individual tube having a diameter of 5 mm or even smaller. Because of their small sizes and high sensitivity it is possible to achieve good time resolution. A collaboration named NIH has been building PET scanner using low cost LWS. They have developed a 50 straw 50 x 4.4 x 19 cm^3 module with two different configurations: Breast PET configuration and Small animal configuration as it is shown in Fig.3.5.

Figure 3.4: A close-packed array of 20 tubes bonded together [51].

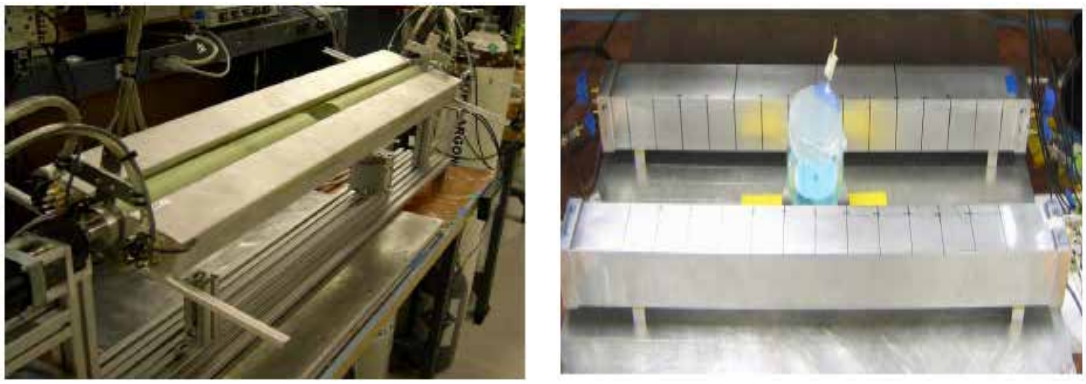

(a) (b)

Figure 3.5: (a) Small Animal PET [52] configuration. (b) Breast PET configuration [52].

Using LWS it is possible to do precise 3D imaging with the possibility of large angular acceptance and parallax-free imaging.

3.2.3 The Resistive Plate Chamber PET detector

Recently there have been made studies to exploit unique characteristics of Gas-based detectors in Positron Emission Tomography (PET). One of such possibility is to construct a Resistive Plate Chamber (RPC) PET detector [53, 54]. It is one of the cost effective solution with respect to crystal based PET scanners with high efficiency, better resolutions. A basic unit of RPC consist of two resistive plates with a single gas gap (SG) between them and separated by insulator spacers. One can assemble more than one such units to form a structure. An RPC detects the charged particles directly and needs no readout of PMTs. They can be built as large as 3 m x 3 m. Furthermore, their capability of induc-

ing a very fast signal of about 4-5 ns , makes them important devices for time-of-flight measurements. In Fig.3.6 schematic view of single gap (SG) and double gap (DG) RPC unit is shown.

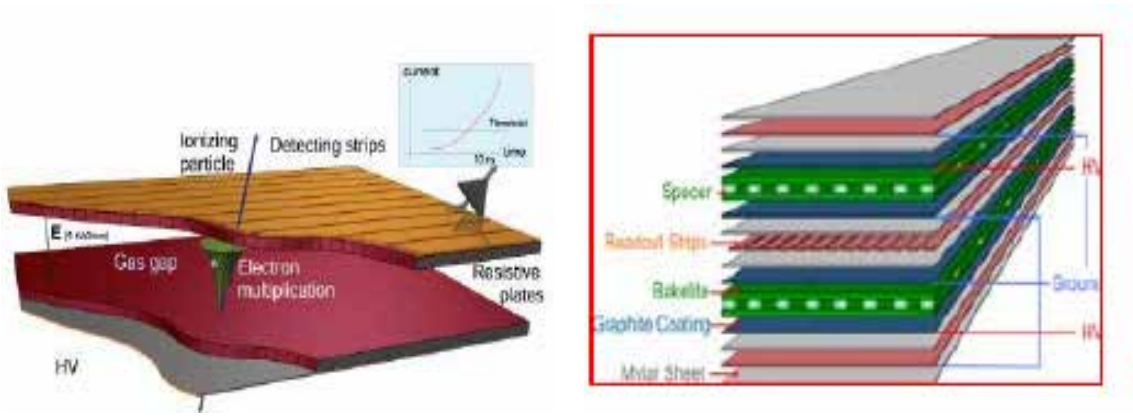

(a) (b)

Figure 3.6: (a) Basic RPC unit consist of two resistive plates with a single gas gap (SG) of about 2 mm wide between them. Signal is produced by avalanche of ionized electrons by a high, uniform electric field of typically 4.5 kV/mm and readout by means of capacitive coupling of metallic strips on the external side of the electrodes [53]. (b) Double Gap (DG) structure with readout strips in between [53].

3.3 The J-PET Prototype

3.3.1 Design and physics behind J-PET

The novel J-PET prototype is an axially symmetric detecting system made up of long strips of organic scintillators (plastic) arranged in cylindrical order as shown in Fig.3.7. The J-PET scanner is the first of its kind, which use organic scintillators despite of their low density and small atomic number (Z). The main gamma quanta detection reaction in organic scintillators is the Compton scattering. On the positive side, organic scintillators have long light attenuation length (about 2 meters) which allows to make a large diagnostics chamber (up to 2 meters long) with sufficient light output (about 10000 photons/MeV) in comparison to crystal scintillators with a light attenuation length of about $\sim$22 cm [6, 7].

To each strip of scintillator a pair of photomultiplier is connected as shown in Fig.3.7(a). Photomultipliers are connected at the end of the strips allowing to use more layers of scintillators and hence the low detection efficiency of plastic scintillators may be compensated by the number of layers and the increased geometrical acceptance by the application of long strips. Configuration of the J-PET scanner allows each detector pair to be in coincidence.

The response time of signal in organic scintillators is fast and J-PET utilizes this potential to determine the point of annihilation. The expected spatial resolution one can obtain with the J-PET scanner is comparable with the current PET scanners.

(a)

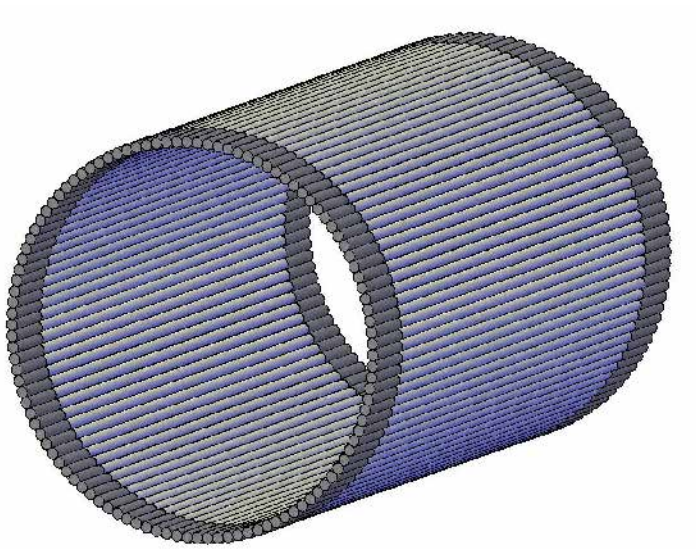

(b)

Figure 3.7: Pictorial representation of the J-PET system. (a) shows a strip of organic scintillator connected to a pair of PM tubes. (b) shows arrangement of these strips with large field of view (FOV) .

Further comparison between the key parameters of commercial and J-PET tomograph is mentioned in Tab.3.1 and the comparison between the characteristics of crystal and plastic scintillators is given in Tab.3.2.
In plastic scintillators signal decay time is less than 2 ns which enhance their time properties (as the time resolution depends on the ratio of number of photo-electrons produced in the detectors to the duration of signal) and helps in effective reconstruction of image taking into account information of TOF [12]. Schematic view of the method for TOF calculation is shown in Fig.3.8.

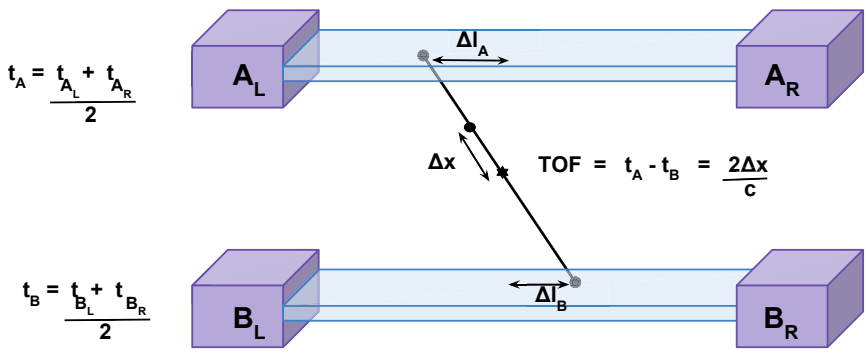

Figure 3.8: Schematic view of the method for TOF calculation in J-PET detector. Star represents the center of LOR and dot depicts the annihilation point. Δl indicates the distance of hit position from the center of scintillator along its length and Δx indicates the distance between point of annihilation and center along LOR.

Table 3.1: Comparison between commercial PET scanners [1,2] and J-PET prototype [55].

	Philips (Ingenuity TF)	GE (Discovery 710)	Siemens (Biograph mCT Flow)	Philips (Vereos)	J-PET
Detector material	LYSO	LYSO	LSO	LYSO	EJ-230
Photo-detector	PMT	PMT	PMT	dSiPM	PMT
Scintillator size (mm^3)	4x4x22	4.2x6.3x25	4x4x20	4x4x22	7x19x500
Number of scintillators	28,336	13,824	32,448	23,040	192
Number of PMTs	420	256	768	-	384
Axial FOV (cm)	18	15.7	21.8	16.3	50

Table 3.2: Properties of crystals and plastic scintillators used in commercial tomograph and J-PET module, respectively [4–7].

Name	Type	Density [g/cm^3]	Light output [photons/MeV]	Attenuation length cm	Decay time [ns]
BGO	crystal	7.13	6000	22.8	300
LSO	crystal	7.4	29000	20.9	42
LYSO	crystal	7.3	18000	20.9	50
BC-420	polymer	1.032	10240	110	1.5
EJ-230	polymer	1.023	10240	120	1.5
BC-404	polymer	1.032	10880	160	1.8
BC-408	polymer	1.032	10240	380	2.1

Chapter 4

The two strip J-PET prototype

In order to validate the hit-time and hit-position reconstruction method which will be presented in this thesis (explained in chapter 5) double strip J-PET prototype was used, as it allows for simultaneous registration of two annihilation quanta and reconstruction of both LOR and TOF.

4.1 Experimental setup

The prototype was built out of two scintillators wrapped with 3M Vikuiti specular reflector foil [56]. The strips were read out by Hamamatsu photomultipliers R9800 [36] connected optically to the most distant ends of scintillators via optical gel EJ-550. Serial Data Analyzer (Lecroy SDA6000A) was used to readout the output of the photomultipliers. ^{22}Na isotope was used as a source of annihilation gamma quanta. For noise suppression and selection of annihilation gamma quanta a coincident registration of signals from both detectors was required.

The experiment was carried out with two different set-ups of double strip J-PET prototype. The difference between them was the use of scintillators with different dimensions and type.

- Two BC-420 [4] strips with dimensions 300 x 19 x 5 mm^3
- Two EJ-230 [5] strips with dimensions 500 x 19 x 7 mm^3

The measurements with each set-up were done in 3 steps:

- Scan of whole strips along their length by irradiating them with a collimated beam of annihilation quanta (FWHM ~1.5 mm [57]) with a step of 3 mm using a dedicated mechanical system. Collimated beam was produced by ^{22}Na β^+ source located within a lead collimator with 1.5 mm wide and 20 cm long slit. General scheme of experimental setup is shown in Fig.4.1 and real setup arrangement is shown in Fig.4.2. In this case gamma quanta were hitting the scintillator perpendicular to it.
- Measurements by rotating the collimator with an angle θ(15^0 and 30^0) in clockwise and anti-clockwise directions at the central hit-position of scintillator only. In this case gamma quanta were hitting the scintillator obliquely.

- Measurements with bare source instead of collimated one i.e. unrestricted 4π direction of emission. Different configuration of bare sources were used. Detailed explanation of those configurations are given in chapter 8.

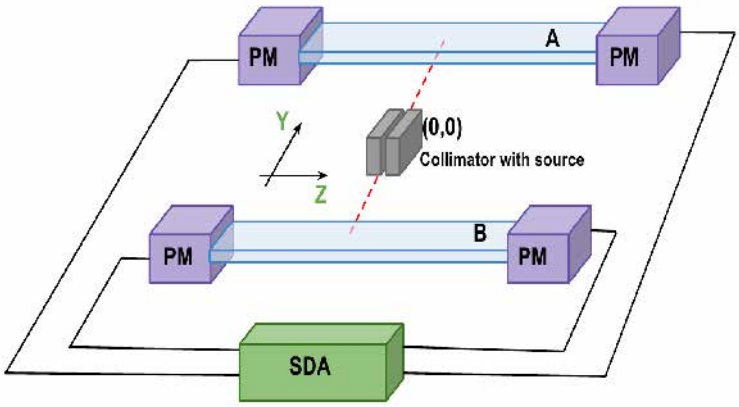

Figure 4.1: A schematic view of the double-strip J-PET prototype built for scan measurements. Both the scintillators were 41 cm apart from each other along Y-axis and from the position of source located within a collimator each of them are at a distance of 20.5 cm along Y-axis.

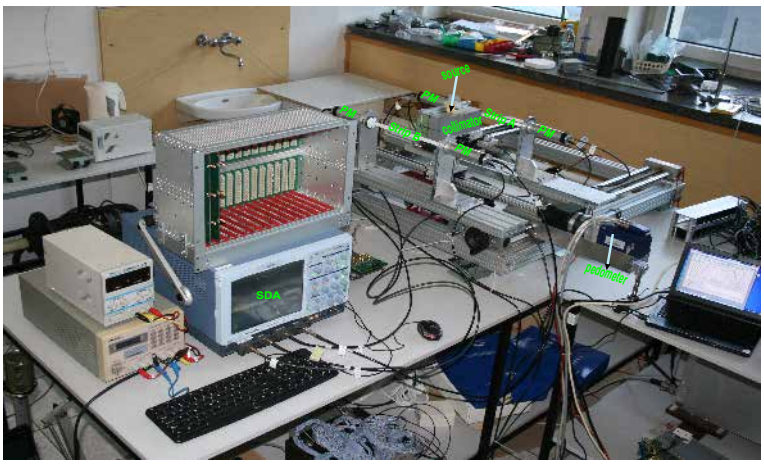

Figure 4.2: Real set up of the double-strip J-PET prototype built out of two scintillators wrapped with 3M Vikuiti specular reflector foil [56] read out by photomultipliers using Serial Data Analyzer. A collimated beam of annihilation gamma quanta was used to irradiate the scintillators.

4.1.1 Format of collected data

For each setting high statistics of signals correspond to each hit-position of gamma quanta was collected from the four photomultipliers probed with interval of 100 ps by means of

Serial Data Analyzer (Lecroy SDA6000A). Each signal was saved in the form of ASCII files. Exemplary sampled signals obtained from the four photomultipliers at three different irradiated positions are shown in Fig.4.3.

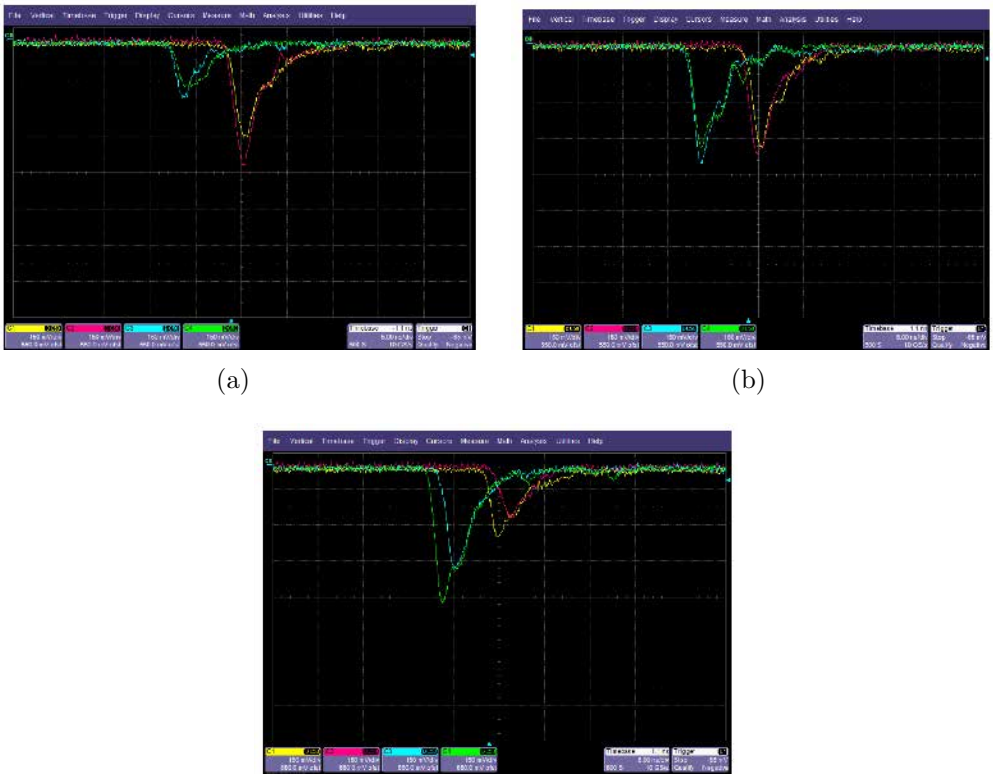

(a) (b)

(c)

Figure 4.3: Exemplary signals measured at three different hit-positions from all the four photomultipliers. Yellow and blue solid lines represent the signals measured from left and right photomultipliers of strip A (see Fig.4.1). Pink and green solid lines are the signals measured from left and right photomultipliers of strip B (see Fig.4.1). In all the figures C1, C2, C3 and C4 are the channels of SDA connected to these photomultipliers with their time and voltage scale information. (a) Measured from the position when gamma quanta hit the strips near to their left ends (see Fig.4.1). (b) When the position of irradiation was in the proximity of center of the strips (see Fig.4.1). (c) When the annihilated photons were hitting the strips nearer to their right ends (see Fig.4.1).

4.2 Correction and selection of data

4.2.1 Pedestal correction

After collection of data a primary correction was implemented on the registered signals in order to create a signal library free of the electronic voltage offset referred to as Pedestal correction. To perform this, the average value of voltage in the noise region, encircled by the red area in Fig.4.4(a) was calculated. Then this computed average was used for

pedestal correction for that particular signal. An exemplary signal without and with pedestal correction is presented in Fig.4.4.

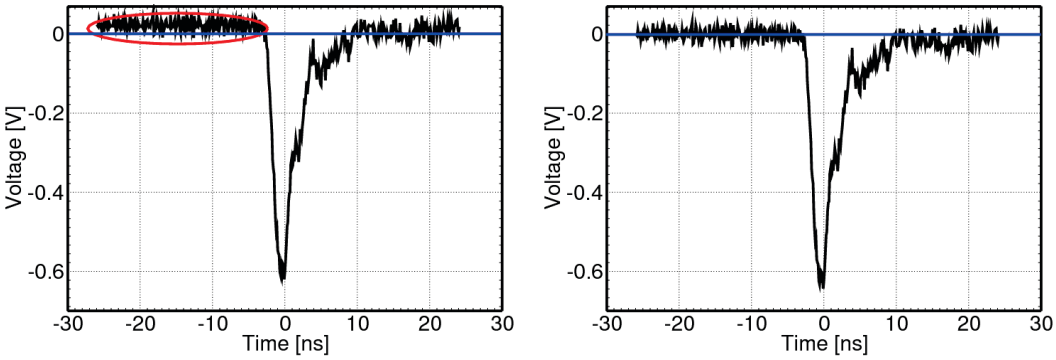

Figure 4.4: (a) Example of a measured signal without pedestal correction. (b) The same signal with pedestal correction.

4.2.2 Data Selection

In plastic scintillator detection of 0.511 MeV gamma quanta is based on Compton scattering. In Fig.4.5 simulated energy distribution of Compton scattered electrons for three different primary energies of gamma quanta is shown. The chosen energies correspond to the annihilation quanta (511 keV) which were scattered in the patient's body by the angle 0^0, 30^0 and 60^0. Thus, Fig.4.5 shows the energy spectra expected for the gamma quanta which were scattered in the patient's body under these angles.

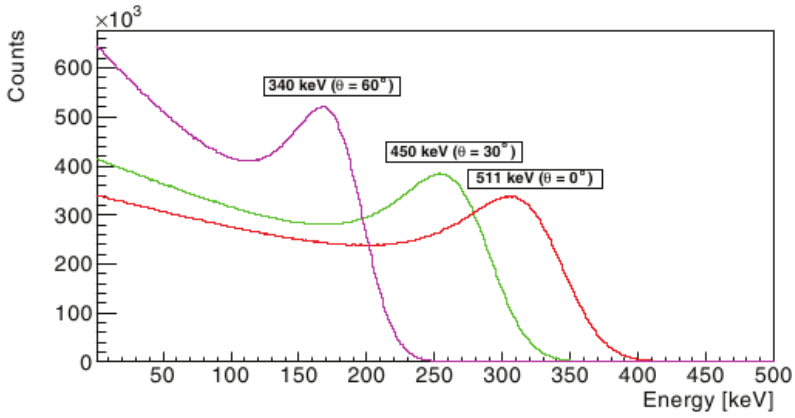

Figure 4.5: Energy distribution of Compton scattered electrons for three different primary energies of gamma quanta scattered at different angles. The spectra were simulated taking into account energy resolution of the J-PET detector [8]

It is clear from Fig.4.5 that in order to limit the registration of scattered gamma quanta in patient within the angular range 0^0 to 60^0 (as it was applied earlier e.g. in some

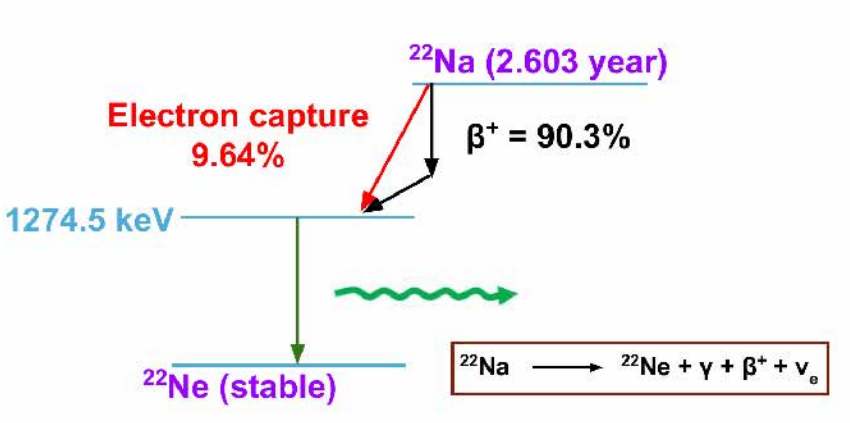

Figure 4.6: Decay scheme of ^{22} Na radioactive source.

LSO or BGO based tomographs [58]), a low energy threshold of about 0.2 MeV [12] has to be applied. Application of such threshold suppresses most of those events which originate from secondary Compton scattering in the patient's body and blur the reconstructed image. Moreover, application of the threshold at 0.2 MeV level reduces almost to the negligible level events with multi Compton scattering in the detector [59]. Signals with energy higher than 0.38 MeV were also discarded in order to limit the registration of 1.2 MeV gamma quanta produced in the decay of ^{22}Na isotope (see Fig.4.6) and also to limit the effect of cosmic rays which can blur the reconstructed image.

So, an initial filtering was performed by considering only those events for which energy depositions were in the range from 0.2 MeV to 0.38 MeV. Relation between the measured charge and deposited energy was computed by fitting the KleinNishina formula [60] convoluted with the detector resolution to the experimental data. The fit was performed using energy resolution (β), energy calibration constant (α) and normalization constant (A) as free parameters [61]. A fit was constructed with Neyman χ^2 statistics defined as follows:

$$\chi^2(\alpha, \beta, A) = \sum_i \frac{(A * N_{sim}(i, \alpha, \beta) - N_{\exp}(i))^2}{N_{\exp}(i)} \tag{4.1}$$

where, i denotes the ith bin of the histogram N_{exp}.

Blue line in Fig.4.7 represents the experimental spectra obtained by irradiating the scintillator with a collimated beam of annihilation gamma quanta at its center. The red in Fig.4.7 indicate the distribution simulated based on the Klein-Nishina [60] formula convoluted with the detector resolution. In low energy region experimental spectra shown in Fig.4.7 is not reproduced by simulated spectra because of: the triggering condition which accept only those signals which have amplitude smaller than -80 mV and the defined energy range for fitting parameters which is from 0.2 MeV to 0.38 MeV.

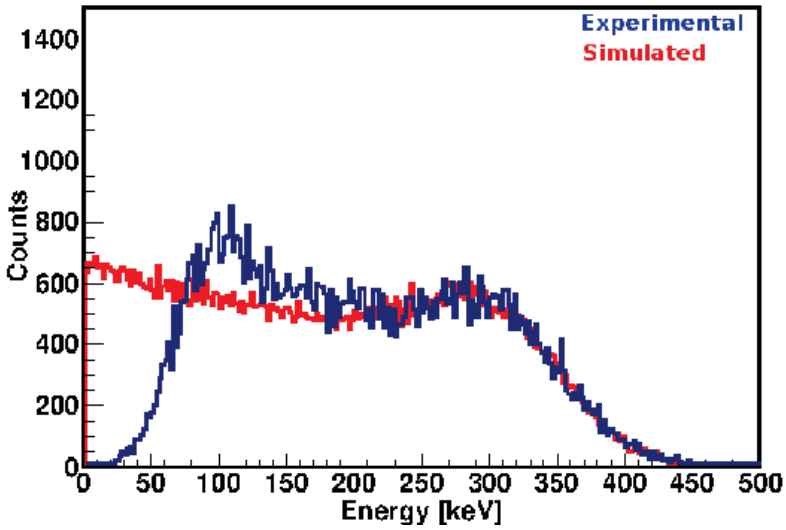

Figure 4.7: Experimental and simulated energy distribution of scattered electrons via Compton effect for gamma quanta carrying energy of 511 keV. Superimposed lines red and blue, indicate the distribution simulated based on the Klein-Nishina [60] formula convoluted with the detector resolution and the distribution obtained experimentally, respectively.

Chapter 5

Hit-position and hit-time reconstruction method based on library of model signals

During examination of patient using the PET technology, a pair of gamma quanta is emitted as a result of positron-electron annihilation process and it is detected by pair of detectors aligned opposite to each other. The interaction time and hit-position of these gamma quanta allows to reconstruct a line of response, a line along which the annihilation quanta are propagating and which includes the point of annihilation of positron emitted from the radio-pharmaceutical tracer inside the patient's body. In this chapter a basic idea of hit-position and hit-time reconstruction used in the J-PET scanner is presented.

5.1 Working principle of hit-position and hit-time reconstruction method

Signals collected with the photomultipliers connected at the ends of scintillators changes their shape and amplitude with the hit-position along the length of strip as it is shown in Fig.4.3.

The changing of signal's shape with respect to hit-position is basic idea for database-search reconstruction method. One possible way to reconstruct the hit-position of gamma quanta is to create a database of synchronized model events [1]. Then compare the registered event with the events stored in the database. The degree of similarity between the registered and database events for a set of well-defined positions along the scintillator will provide the information about the hit-position and hit-time of gamma quanta. The hit-time and hit-position of registered event is defined as a known hit-time and hit-position of the most similar event in the database. In Fig.5.1 a schematic illustration of the working principle behind the presented reconstruction method is shown.

Events are represented as sets of points in a 2-dimensional metric space. The discrete representation of analog signal can be done in two ways: in the **time domain sampling**

[1] An event is a set of two signals measured by a pair of photomultipliers connected at the ends of scintillator, as a results of one particular gamma quanta interaction in the scintillator strip.

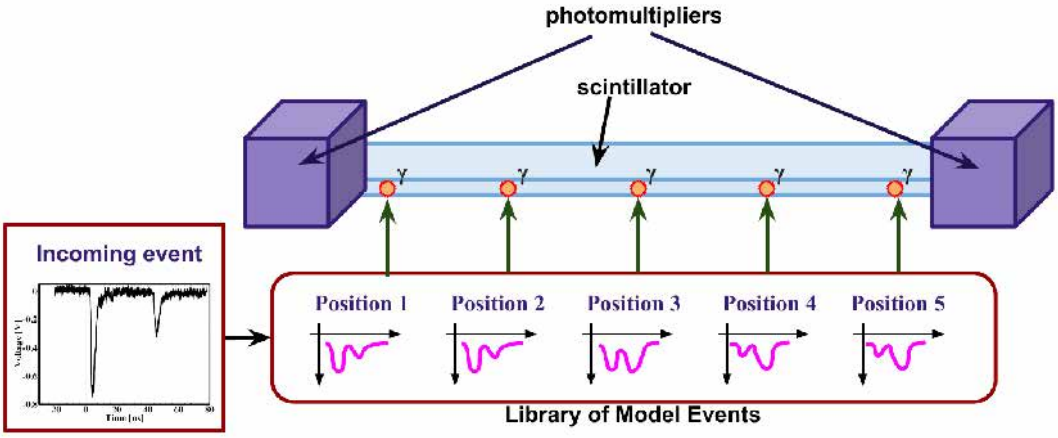

Figure 5.1: A schematic representation of the presented reconstruction method.

or in the **voltage domain sampling**. In the time domain sampling voltage is measured at a given number of points on the time scale as shown in Fig.5.2(a)

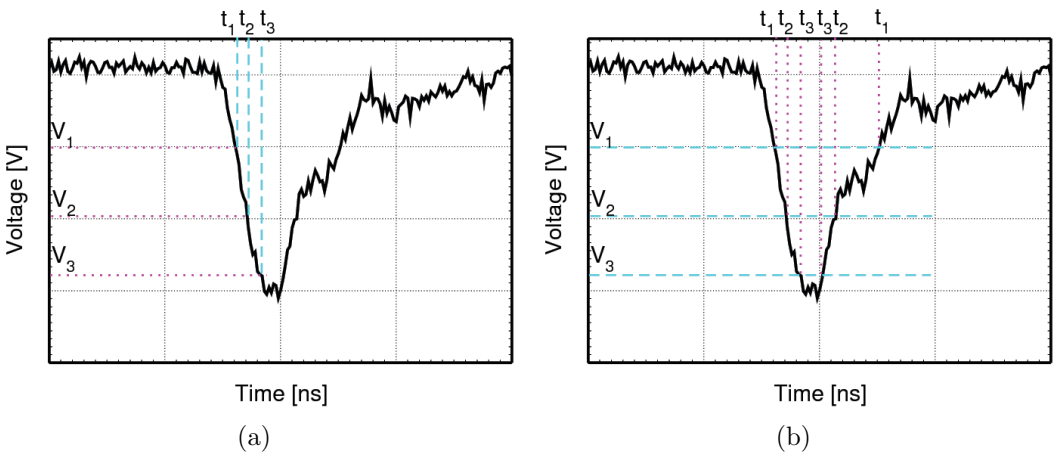

Figure 5.2: (a) Pictorial representation of signal sampling in time domain. (b) Pictorial representation of the same signal sampled in voltage domain.

In the voltage domain sampling: time is calculated at the selected voltage levels (threshold levels) when the signal crosses them as shown in Fig.5.2(b). For the reconstruction method used in the J-PET voltage domain approach has been chosen. Thus, in the J-PET tomograph signals will be sampled by means of multi-threshold constant-level discriminators [62]. In the measurements analyzed in this thesis full signals were sampled by means of Serial Data Analyzer. However, in order to simulate real J-PET tomograph conditions sampling in the voltage domain will be emulated.

5.2 Distance metrics

A distance metric is defined as a function D : A × A → R over a vector space A if for all vectors ∀ $\vec{a_i}$, $\vec{a_j}$, ∈ A and the D($\vec{a_i}$,$\vec{a_j}$) tells about the distance between them. The metrics should have the following properties:

$$D(\vec{a_i}, \vec{a_i}) = 0$$

$$D(\vec{a_i}, \vec{a_j}) = D(\vec{a_j}, \vec{a_i})$$

$$D(\vec{a_i}, \vec{a_j}) + D(\vec{a_j}, \vec{a_k}) \geqslant D(\vec{a_i}, \vec{a_k})$$

$$D(\vec{a_i}, \vec{a_j}) \geqslant 0$$

In a distance function events are considered as a set of points sampled in 2N dimensional metric space. 2N indicates that an event is composed of two signals originating from the extreme ends of scintillator. The two signals of an event are collectively considered as one dataset as the time difference between them is correlated with the interaction point of gamma quantum along the scintillator [11]. Comparison between a pair of events is performed by shifting them in time with respect to each other so that they get maximally aligned. Fig.5.3 illustrates an example of the shifted events.

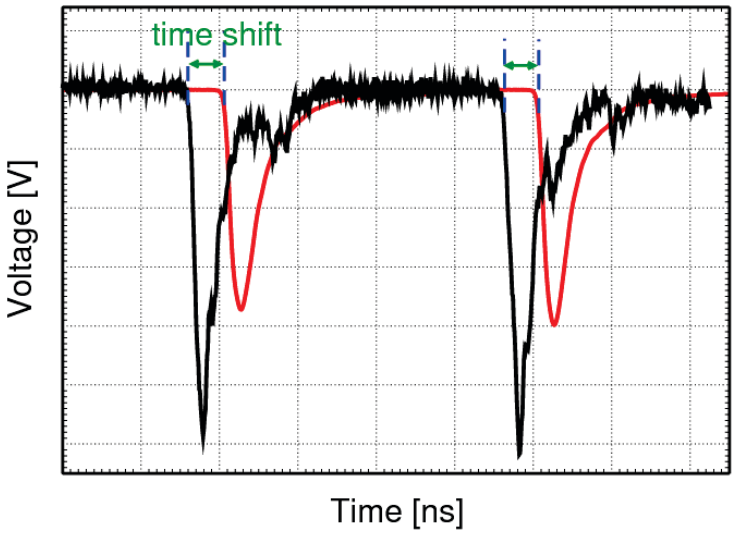

Figure 5.3: Comparison between the two events (registered and reference from database) in the voltage domain. The time difference between them was computed and it is named as time shift. The registered event (solid black line) was shifted by this time shift. In the alignment procedure such time shift is chosen for which registered event and reference event (solid red line) are maximally aligned.

Two methods to measure the similarity has been chosen in order to align the events: Chi-square test and Mahalanobis metric.

5.2.1 Chi-square test

Chi-square is a statistical test commonly used to compare observed number of cases with expectations. Observed cases are obtained empirically through direct observations and expected cases are developed on the basis of some hypothesis. The deviation between the two shows the "goodness of fit" between them. In general, the chi-square statistic is defined as :

$$\chi^2 = \sum_{i=1}^{k} \frac{((observed)_i - (\exp ected)_i)^2}{(\exp ected)_i} \tag{5.1}$$

where k is the number of possible outcomes.

5.2.2 Mahalanobis metric

Mahalanobis distance was first proposed by an Indian statistician P. C. Mahalanobis in 1936 [17]. It is a distance measure originated from an analysis of the deviation in the mean values of different variables in multivariate analysis with the consideration of correlation between them. As a discriminant analysis method, it is useful in determining the similarity between an unknown and known dataset. Because of the following properties it is considered to be superior to other multivariate distance measures:

- Correlation between the variables is used in its calculation.
- It is very sensitive to intervariable changes in the reference data.
- It is not affected by the dimensionality of the dataset.

It is defined as:

$$D_{Mahalanobis} = \sqrt{D} = \sqrt{(x-\mu)S^{-1}(x-\mu)^T} \tag{5.2}$$

where,

- $\mathbf{x}$ is a row vector
- μ is a vector of means of the sample
- $\mathbf{S}$ is the variance-covariance matrix of the sample. It diagonal elements are the variances of each variable and off diagonal are the covariances.

It is a weighted Euclidean distance where the weighting is determined by the range of variability of the sample point expressed by the covariance matrix.

5.3 Reconstruction method

The algorithm used to reconstruct the hit-position and hit-time was divided into following steps:

- To create a library of synchronized model events in order to have same hit-time value for all events

- To reconstruct the hit-position and hit-time of measured event by performing the comparison between the measured(i.e. registered) and model events using Mahalanobis distance

Detailed explanation is given in the following sections.

5.3.1 Library of synchronized model events

The reconstruction method explained in the present work demands the creation of a database consisted of synchronized model events for various interaction points. The library of synchronized model events was produced by performing a scan of the scintillator strip (i.e the model events are obtained experimentally, they form set of representative events). The scintillator strips were irradiated with the collimated source of annihilation gamma quanta along its length i.e. along the z-axis (see Fig.4.1). Collimated beam is produced by placing the source inside a collimator with a spacial profile width of FWHM equal to 1.5 mm [57]. In order to assign the place of irradiation to each measured event, movement of the collimator must be synchronized with the data acquisition system. The information about the position of irradiation is added to each event in the library. For each irradiated position a high statistics was collected and these events were used to establish the model events.

5.3.1.1 Synchronization of signals

Synchronization of signals is needed in order to have the same hit-time value for all events in the library with gamma quantum hitting the detector at a certain position. This was done by shifting their time scales by an appropriate calibration constant. For each event this constant needs to be determined separately. It can be defined as

$$t_{synch} = \frac{t_L + t_R}{2} \tag{5.3}$$

where t_L and t_R denote the beginning[2] of the signal measured at the left and right sided photomultipliers connected to the ends of the scintillator, respectively.

After the transformation $t_L + t_R = 0$ as shown in Fig.5.4, implies that after transformation always one among the pair (t_L , t_R) is negative and the other positive. As it will be shown later in Section 5.3.2, this procedure of synchronization allows to determine not only LOR but also TOF for each registered event [63].

[2]The beginning of the signal we defined as the time value at which the signal crosses the defined threshold value (in this case it is -80 mV).

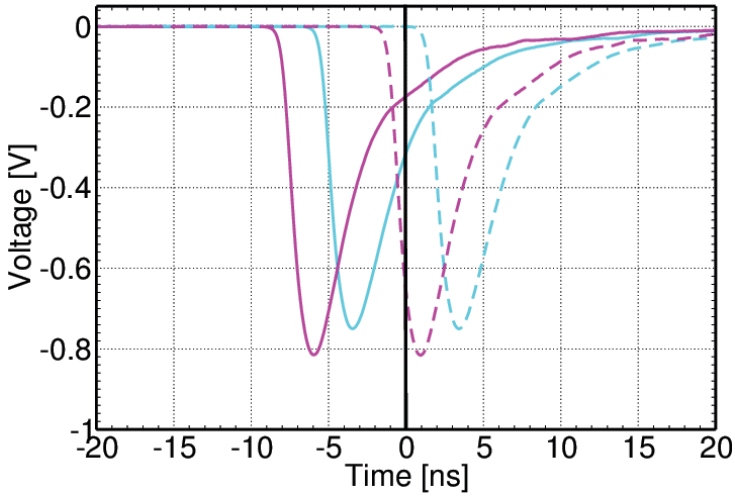

Figure 5.4: Representation of signals measured from a pair of photomultipliers connected to both ends of a scintillator. Solid pink and cyan lines represent the left and right signals measured by left and right PMs, respectively. Dotted pink and cyan lines represent the same left and right signals, respectively, synchronized with the implementation of t_{synch}.

5.3.1.2 Determination of model events shape

Due to the low density of plastic scintillator the gamma quanta interact with it nearly only via Compton effect hence, signals amplitude vary from event to event. Therefore one need to elaborate a method to determine an average shape of signals originating from the interaction at a given hit-position. This is done in two steps:

- Determining an average event
- Computing the χ^2 statistics in order to perform event's alignment.

Determination of average event: Approximate shape of the model event at a given hit-position was determined by averaging the signals measured [18]. The calculated average event was treated as a reference in order to align the measured events shown in Fig.5.5. For every hit-position it was calculated separately. Such kind of alignment is necessary to suppress spread of the events in terms of amplitude as well as time.

Event's alignment: The χ^2 statistics was defined for each measured event in order to perform the event's alignment. It was done by comparing leading edge of the database and computed average signals in the following form:

$$\chi^2(\delta t, \alpha_{L,}\alpha_R) = \sum_{i=1}^{n} \frac{\left(t_{AvgLeft}(V_i) - t_{dbLeft}(\alpha_L V_i) - \delta t\right)^2}{n} + \sum_{i=1}^{m} \frac{\left(t_{AvgRight}(V_i) - t_{dbRight}(\alpha_R V_i) - \delta t\right)^2}{m} \tag{5.4}$$

where δt is the time shift along time axis and α_L, α_R are normalization factors for signals (left and right) registered at both ends of scintillator. $t_{AvgLeft}(V_i)$ and $t_{AvgRight}(V_i)$ denote time of left and right average signals computed for voltage V_i at their leading edge.

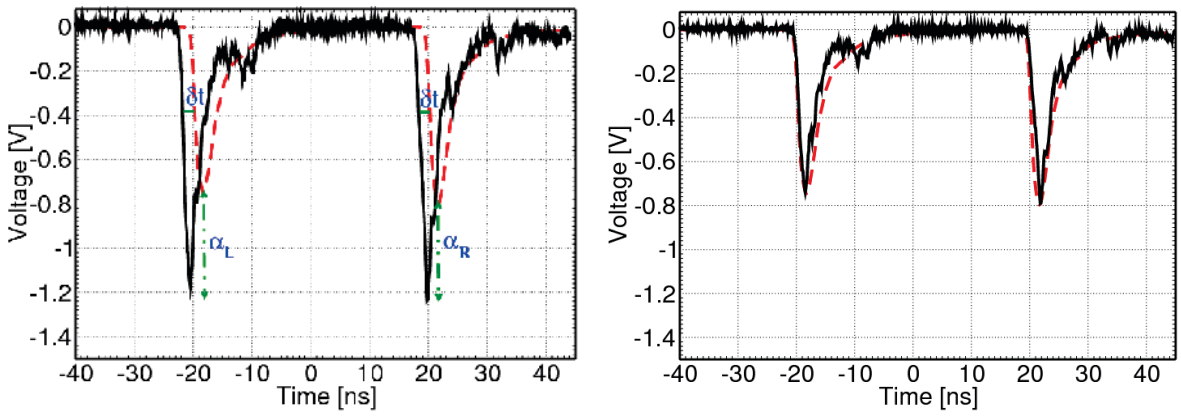

(a) (b)

Figure 5.5: (a) Example of database events before the alignment to average signals. (b) The same database events after the alignment to average signals. Black curve represents measured events while the red represents computed average events

$t_{dbLeft}(\alpha_L V_i)$ and $t_{dbRight}(\alpha_R V_i)$ is the time computed for rescaled left and right signals at their leading edge, respectively [18]. n and m are the number of points sampled at the leading edge of the left and right signals, respectively.

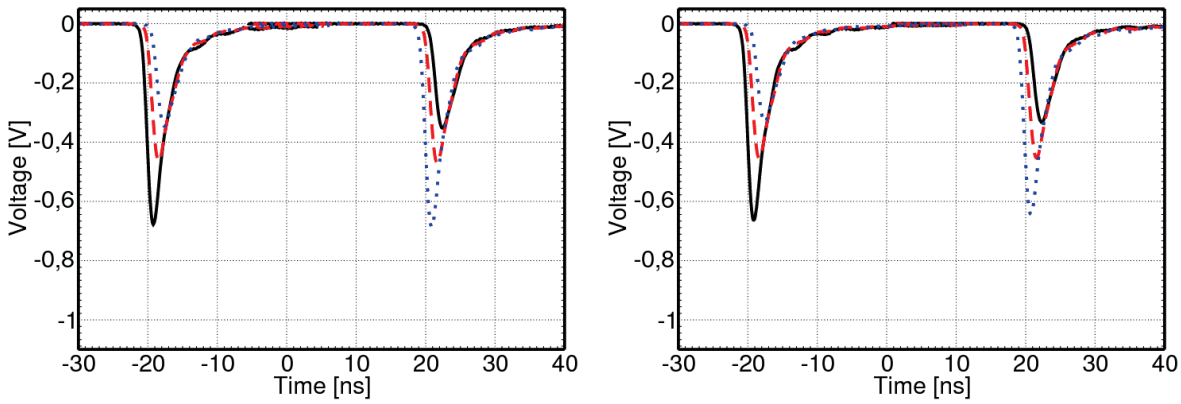

(a) (b)

Figure 5.6: (a) Exemplary sample of model signals at three different irradiated positions along the length of strip A and B (see Fig.4.1). Black solid line is the model event produced for the position nearer to the left end of the strip. Red dashed line is the model event belongs to the central hit-position. Blue dotted line is the model event for the position lying in the proximity of right end of the strip. (a) Model events for strip A. (b) Model events for strip B.

The best alignment between the two compared events is obtained by minimization of χ^2 value. The values of fitted parameters α_L, α_R and δt corresponding to the minimum value of χ^2 were used to rescale the database signal. Then average of these rescaled events was computed again resulting in so called model event. Example of model events at three

different hit-positions along the length of strip A and strip B (see Fig.4.1) are shown in Fig.5.6.

5.3.2 Reconstruction of hit-position and hit-time

Reconstruction of gamma quanta hit-position is done by comparing the measured events with each model events stored in the library at a defined threshold levels using Mahalanobis distance as a measure of similarity, defined as

$$M.D(z, \Delta t) = \sqrt{(\vec{x}(z, \Delta t))(cov\ matrix(z))^{-1}(\vec{x}(z, \Delta t))^T} \tag{5.5}$$

where, z represents the hit-position along the scintillator strip and Δt is the shift in time between the two compared events. Values of z and Δt corresponding to the most similar model event will be returned as a result of comparison. The most similar model signal will be chosen as the one for which the value of Mahalanobis distance will reach the minimum. Formulation of covariance matrices and $\vec{x}$ used in Eq.5.5 is explained in section below.

5.3.2.1 x - vector

$\vec{x}$ used in the definition of the Mahalanobis distance Eq.5.5 is a difference between the time values (obtained at the defined threshold level) of the measured event vector and the model event vector shifted by Δt as mentioned in Eq.5.6.

$$\vec{x}_k(z, \Delta t) = \vec{t_k} - \vec{t}_{model}(z) - (\Delta t) \tag{5.6}$$

k enumerates events in the database. $\vec{t_k}$ represents the vector of kth measured event for a tested hit-position, whereas $\vec{t}_{model}$(z) represents the vector of model event for hit-positions z of gamma quanta along the length of scintillator. It was calculated only for tested position. Number of elements in $\vec{x}$ depends on the number of threshold levels m applied to the signals of an event. An ith element of $\vec{x}$ is defined as :

$$x_{k(i)}(z, \Delta t) = t_{k(i)} - t_{model(i)}(z) - (\Delta t) \tag{5.7}$$

where, $t_{k(i)}$ and $t_{model(i)}$(z) are the elements of $\vec{t_k}$ and $\vec{t}_{model}$, respectively. $t_{k(i)}$ are equal to the respective times defined at the applied thresholds for left and right measured signals. $t_{model(i)}$ are the times at defined thresholds for left and right model signals. Illustration of $\vec{x}(z, \Delta t)$ constructed for single threshold level for a kth event is explained below. Number of elements are 2 i.e.

$$\vec{x}_k(z, \Delta t) = [x_1\ ,\ x_2]_k$$

$\vec{t_k}$ and $\vec{t}_{model}$ are:

$$\vec{t_k} = [t_L\ ,\ t_R]_k$$
$$\vec{t}_{model} = [t_{model_L}\ ,\ t_{model_R}]$$

where, t_{model_L} and t_{model_R} are the time values of model event's left and right signals when they cross the threshold level, respectively. t_L and t_R are the time values of measured event's left and right signals when they cross the threshold level, respectively. So, $\vec{x_k}$ becomes:

$$\vec{x}_k(z, \Delta t) = [t_L - t_{model_L}(z) - \Delta t \ , \ t_R - t_{model_R}(z) - \Delta t]_k$$

Unit of each element is nanoseconds (ns).

5.3.2.2 Covariance Matrix

It was calculated for each hit-position. It contains $(2m)^2$ elements and m is the total number of threshold levels applied to signals at both sides of the scintillator. Its elements are covariances calculated from the time difference between the measured and average events at the defined threshold level.

$$cov_{ij} = \sum_{k=1}^{N} \frac{(\vec{t}_{k(i)} - \vec{t}_{avg(i)})(\vec{t}_{k(j)} - \vec{t}_{avg(j)})}{N} \tag{5.8}$$

Eq.5.8 was used to construct the covariance matrix. k enumerates events in the database, i, j are varied from 1 to m. $t_{k(i)}$ and $t_{k(j)}$ are the elements of $\vec{t_k}$. $t_{avg(i)}$ and $t_{avg(j)}$ are the elements of $\vec{t_{avg}}$. $\vec{t_k}$ represents the vector of measured event at given hit-position, whereas $\vec{t_{avg}}$(z) represents the vector of average event belonging to same hit-position of gamma quanta along the length of scintillator. N is the length of the database corresponding to each hit-position.

As an example covariance matrix for single threshold level is as follows (as stated above, total number of elements is 2^2 i.e equal to 4):

$$cov_{ij} = \begin{bmatrix} a_{11} & a_{12} \\ a_{21} & a_{22} \end{bmatrix}$$

In Fig.5.7 signals (left and right) of measured and average events are shown. Dotted green line represents the applied threshold level to both events. t_L and t_R are the time values of measured event's left and right signals, respectively, when they pass through the threshold level. t_{avg_L} and t_{avg_R} are the time values of average event's left and right signals when they cross the threshold level.

$\vec{t_k}$ and $\vec{t_{avg}}$ for the event shown in Fig.5.7 are:

$$\vec{t_k} = [t_L \ , \ t_R]_k$$
$$\vec{t_{avg}} = [t_{avg_L} \ , \ t_{avg_R}]$$

For multi-threshold time measurement the formulation of $\vec{t_k}$ and $\vec{t_{avg}}$ will be:

$$\vec{t_k} = [t_{1L} \ , \ t_{2L} \ , \ t_{3L} \ , \ .... \ , \ t_{1R} \ , \ t_{2R} \ , \ t_{3R} \ , \ ....]_k$$
$$\vec{t_{avg}} = [t_{avg_{1L}} \ , \ t_{avg_{2L}} \ , \ t_{avg_{3L}} \ , \ .... \ , \ t_{avg_{1R}} \ , \ t_{avg_{2R}} \ , \ t_{avg_{3R}} \ , \ ....]$$

where iL and iR are the time values at i^{th} threshold levels on left and right side, respectively.

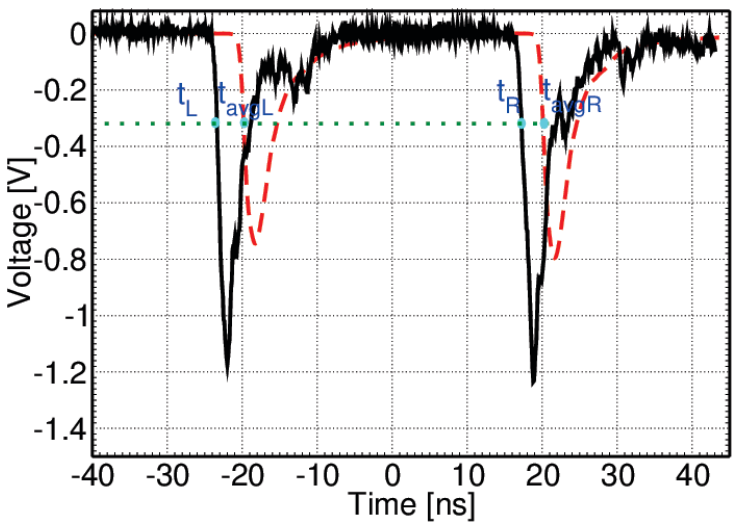

Figure 5.7: An exemplary demonstration of single threshold applied to the measured and average events .

Elements of covariance matrix for the events measured at defined hit-position at single threshold level are:

$$a_{11} = \sum_{k=1}^{N} \frac{[(t_L - t_{avg_L})(t_L - t_{avg_L})]_k}{N}$$

$$a_{12} = \sum_{k=1}^{N} \frac{[(t_L - t_{avg_L})(t_R - t_{avg_R})]_k}{N}$$

$$a_{21} = \sum_{k=1}^{N} \frac{[(t_R - t_{avg_R})(t_L - t_{avg_L})]_k}{N}$$

$$a_{22} = \sum_{k=1}^{N} \frac{[(t_R - t_{avg_R})(t_R - t_{avg_R})]_k}{N}$$

The unit of each element is ns^2.

5.3.2.3 Hit-position

Hit-position reconstructed with this method is the position (z) of most similar model event from the library with respect to measured event for which value of Mahalanobis distance is minimal. This value of z is returned as a result of comparison and called as the reconstructed hit-position. Distribution of difference between the obtained reconstructed hit-position and true hit-position of a tested event (i.e. Δz) gives the spatial resolution mentioned in Eq.5.9. From *true* position we mean the real position of irradiation.

$$\Delta z = z_{reconstructed} - z_{true} \tag{5.9}$$

5.3.2.4 Hit-time and Time-of-flight

The time of particle interaction (hit-time) will be defined as the relative time between measured event and the most similar one from the library. Thus hit-time is equal to the Δt corresponding to the time shift between the two compared events, calculated using Eq.5.5. The TOF of two gamma quanta reacting in detectors A and B is equal to the difference between hit-times in these detectors and may be calculated as

$$TOF = \Delta t_A - \Delta t_B \tag{5.10}$$

This relation may be explained as follows. In general $t_{hit-time}$ is equal to:

$$t_{hit-time} = t + t_{trig}$$

where, t is the measured time of the reaction of gamma quantum in the detector with respect to the time of trigger t_{trig} :

$$t = \frac{t_L + t_R}{2}$$

t_L and t_R denote the beginning of signals measured with respect to the time of the trigger in left and right photomultipliers connected to the detector. In Fig.5.8 registration of generated pulses from an annihilation occurred at a distance of Δx from the center of LOR, in left and right side of detectors A and B is shown. The reconstruction procedure described above returns Δt_A as $t_{hit-time}$ for detector A and Δt_B as $t_{hit-time}$ for detector B (see Fig.5.8). Thus,

$$t_{hit-time_A} = \Delta t_A = t_A + t_{trig}$$

$$t_{hit-time_B} = \Delta t_B = t_B + t_{trig}$$

This provides also determination of the gamma quantum time-of-flight (TOF) [15] which is equal to:

$$TOF = t_{hit-time_A} - t_{hit-time_B} = \Delta t_A - \Delta t_B = t_A - t_B \tag{5.11}$$

It is important to note that the TOF is independent from the time of trigger because the same time of trigger is in effect for both detectors A and B. Hence, the introduced method allows the direct determination of LOR and TOF once the most similar signal to the measurement signal was found in the library of synchronized model signals.

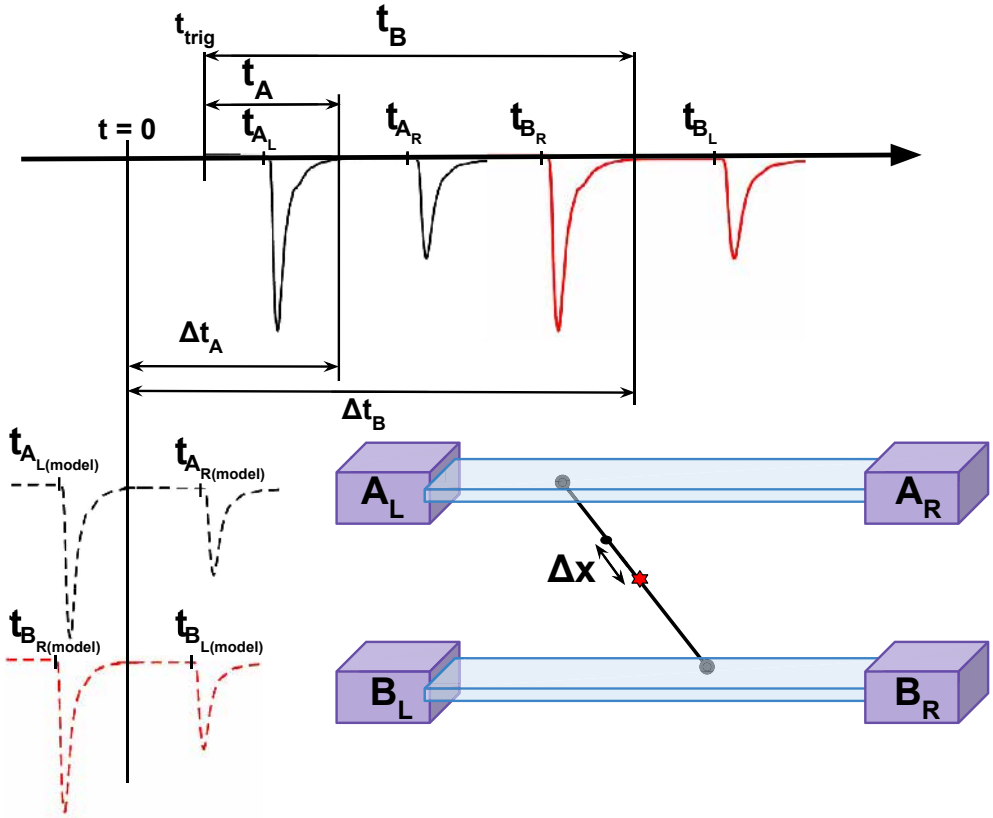

Figure 5.8: Pictorial representation of the method for calculating TOF. Solid black and red lines represent the signals measured from left and right side of detector A and B, respectively. Dotted black and red lines are the synchronized model events from the library of detector A and B, respectively, which are at most similar to the measured events. In the right-lower corner of the figure, an event recorded as a result of annihilation is illustrated. A red star indicates the center of line-of-response, and the dot on the LOR denotes the point of annihilation. A_L, A_R, B_L, and B_R denote the respective photomultipliers connected to left and right sides of detectors A and B. t_{A_L}, t_{A_R} are the beginnings of left and right signals obtained from strip A, respectively. t_{B_L}, t_{B_R} are the beginnings of left and right signals obtained from strip B, respectively. $t_{A_{L(model)}}$, $t_{A_{R(model)}}$ are the beginnings of left and right model signals of strip A, respectively. $t_{B_{L(model)}}$, $t_{B_{R(model)}}$ are the beginnings of left and right model signals of strip B, respectively.

Chapter 6

Optimization of signals processing

Signals obtained from the photomultipliers connected to the scintillators are affected by the noise produced by emission and transmission of photoelectrons by readout electronics and oscilloscope. The noise degrades the accuracy and precision of obtained result (image). Hence, optimization of signal denoising is highly desirable. There are many different approaches for signal denoising.

In the following chapter denoising of signal based on constant level discriminator approach followed with energy deposition classifier using Mahalanobis distance will be explained. Optimization was performed on the data measured by scan of the double strip J-PET prototype mentioned in section.4.1. In the scan of 5x19x300 mm^3 strips the first, central and last irradiated positions (z, y) were (-150, 0) mm, (0, 0) mm and (150, 0) mm, respectively. The conclusions drawn from the procedure of optimization are used as the reference for other data sets measured with same or different dimensions of scintillators.

6.1 Optimization of signals processing from two strips module with dimension of 5x19x300 mm^3 strips

6.1.1 Optimization of constant-level discriminator

In order to design the most optimum configuration of thresholds for the full scale J-PET tomograph it is necessary to determine the most optimum number of thresholds and the voltage value for each threshold. Determination of TOF resolution will be used as a criterion of optimization. The aim of the following section is to find such thresholds configuration for which the TOF resolution is the best. Therefore, the measured events were compared to each stored model events from the library. As a result of each comparison a value of Mahalanobis distance was obtained. Among those values minimal value of Mahalanobis distance was chosen, which represents the maximal alignment of two compared events. Mahalanobis distance is parameterized by two parameters: position z of model event and shift in time Δt between two compared events. Δt is the arrival time of coincident photons inside the pair of strips and TOF is equal to difference between them as mentioned in Eq.5.11. The optimized level is the one at which root mean squared error value of TOF distribution i.e. rms(TOF error) is minimal.

6.1.1.1 Single-threshold level

Comparison between the two events (one is measured and other is from synchronized model library) were performed at single threshold level. Events measured at central hit-position were considered. Exemplary covariance matrix calculated at single threshold level reads:

$$cov\ (z) = \begin{bmatrix} 0.0313\ ns^2 & 0.0099\ ns^2 \\ 0.0099\ ns^2 & 0.2521\ ns^2 \end{bmatrix}$$

Fig.6.1(a) shows an example of TOF distribution obtained at one of the applied single-threshold levels. Fig.6.1(b) represents the rms(TOF error) shown as a function of the applied single-threshold level. In order to get the accurate value of optimized level a quadratic function was fitted to the distribution. As a result for central hit-position the optimal threshold level was found to be equal to -80 mV. This value was considered as a reference for other hit positions.

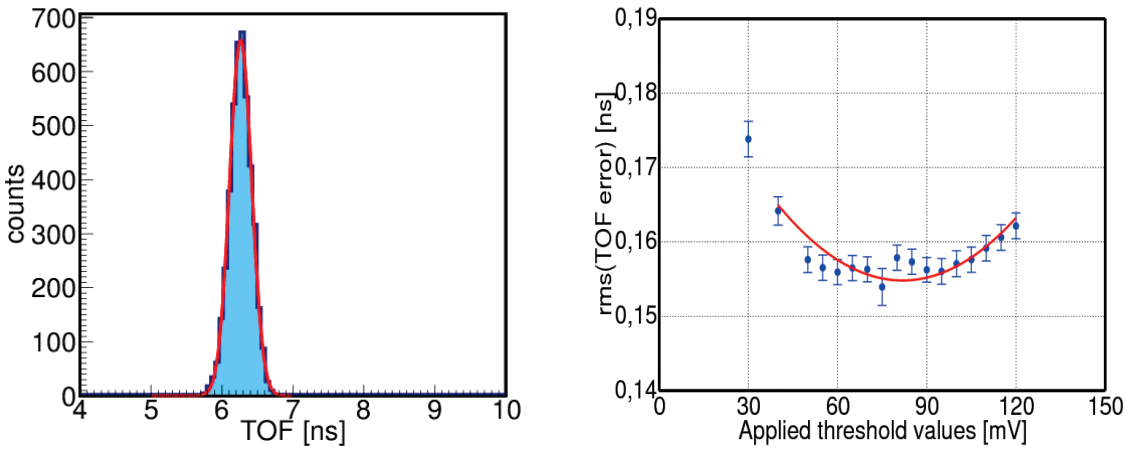

(a) (b)

Figure 6.1: (a) TOF distribution at applied threshold value of -80 mV for central hit-position. (b) The distribution of rms(TOF error) for central hit-position as a function of the threshold level. Circle represents the experimental data and red solid line is the fitted quadratic function.

6.1.1.2 Two-threshold level

As a next step an optimization of threshold levels for the case of two applied thresholds is performed. The test was performed for the signals measured at the center of the scintillator. An exemplary covariance matrix obtained for the two-threshold level reads:

$$cov\ (z) = \begin{bmatrix} 0.0057\ ns^2 & 0.0005\ ns^2 & 0.0019\ ns^2 & 0.0017\ ns^2 \\ 0.0005\ ns^2 & 0.0022\ ns^2 & 0.0008\ ns^2 & 0.0012\ ns^2 \\ 0.0019\ ns^2 & 0.0008\ ns^2 & 0.0344\ ns^2 & 0.0274\ ns^2 \\ 0.0017\ ns^2 & 0.0012\ ns^2 & 0.0274\ ns^2 & 0.3156\ ns^2 \end{bmatrix}$$

Table 6.1: Combinations of two-level threshold applied to the signals.

S.No.	Levels [mV]
1	-50, -80
2	-50, -100
3	-50, -120
4	-55, -90
5	-55, -100
6	-55, -120
7	-60, -80
8	-60, -100
9	-60, -120
10	-65, -100
11	-65, -120
12	-70, -100
13	-70, -120
14	-75, -100
15	-75, -120
16	-80, -100
17	-80, -120
18	-85, -100
19	-85, -120
20	-90, -120
21	-95, -120
22	-100, -120

Different combinations of thresholds listed in Tab.6.1 were tested. Fig.6.2 represents the rms(TOF error) obtained at various combinations of thresholds.

It is observed from Fig.6.2 that the values of rms(TOF error) for combinations 1 to 8 and 10 and 11 listed in Tab.6.1 are consistent within the range of uncertainties. In order to determine the optimized level, TOF distribution was computed for different irradiated positions. Fig.6.3 shows the distribution of rms(TOF error) obtained at different irradiated positions for combinations (2,3 and 5) listed in Tab.6.1. It is clear from Fig.6.3 that the shape of TOF distribution is not changing with different combinations of applied threshold levels. So, -55 mV and -100 mV were chosen as optimum for two-threshold level and the value of time-of-flight obtained for this combination at central hit-position is better than the one obtained from single-threshold level. The test on three-threshold level was also performed.

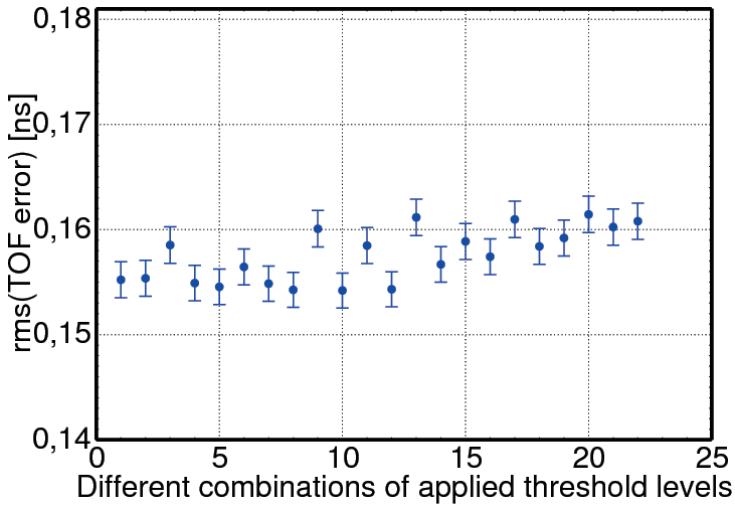

Figure 6.2: TOF resolution for various two-threshold levels applied to signals originating from the irradiation at the central position. On X-axis serial number of applied threshold values (listed in Tab.6.1) are mentioned.

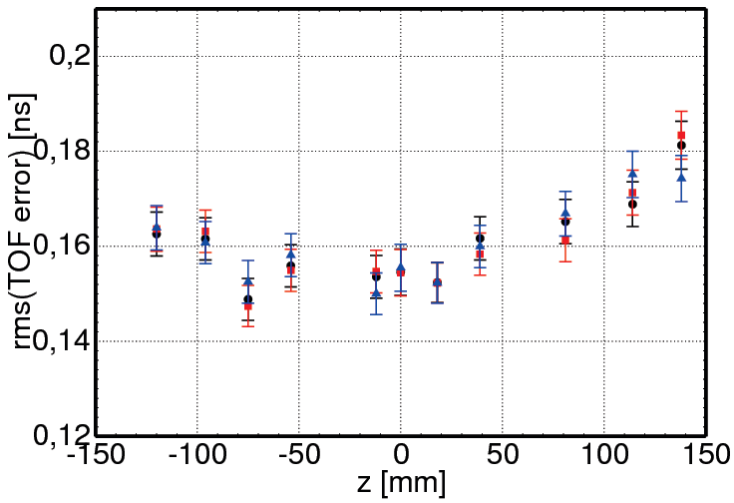

Figure 6.3: Distribution of rms (TOF) at different hit-position for three combinations of two-threshold levels. Black circle shows the distribution when -55 mV and -100 mV thresholds are applied. Red square represents the distribution when -60 mV and -90 mV threshold are applied. Blue up-triangle indicates result for -55 mV and -70 mV threshold value.

6.1.1.3 Three-threshold level

Signals were sampled at different combinations of three-threshold levels. The combinations are shown in Tab.6.2. It was found that there is no significant improvement in time-of-flight with increasing number of threshold levels from 2 to 3. This is as expected because a signal is composed of many single photoelectron signals and only the first few photoelectrons contribute to the onset of the leading edge of photomultiplier signals [8]. Thus, the timing information carried out by the leading edge of the signal is determined by only few photoelectrons and the values of the times measured at different thresholds become strongly correlated. So, for further analysis, two-threshold level with values -55 mV and -100 mV will be used as optimized constant level discriminator.

Table 6.2: Combinations of three-level threshold applied to the signals.

S.No.	Levels [mV]
1	-40, -60, -80
2	-40, -60, -90
3	-40, -60, -100
4	-40, -60, -110
5	-40, -60, -120
6	-40, -70, -120
7	-50, -70, -80
8	-50, -70, -90
9	-50, -70, -100
10	-50, -70, -110
11	-50, -70, -120
12	-50, -80, -120
13	-50, -90, -120
14	-60, -80, -100
15	-60, -80, -120
16	-60, -90, -120
17	-70, -90, -120

6.1.2 Optimization of energy deposition

As it is mentioned in Chapter 4.2 suppression of signals with low energy deposition improves the quality of reconstructed image. An exemplary deposited energy distribution of signals obtained at central hit position from the PMs connected to the extreme ends of the scintillator is presented in Fig.6.4. The time resolution and hence the covariance matrix depends on the number of photoelectrons in the signal and hence on the energy deposited by the interacting photon. Therefore the comparison of signals should improve if the covariance matrix would be established as a function of the energy loss. To check this we will first divide the range of available energy losses into two regions.

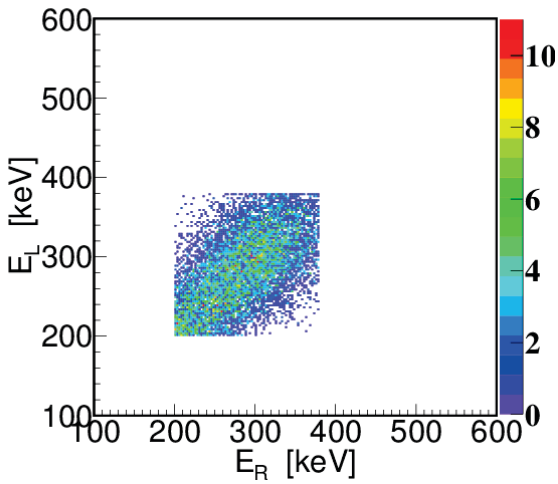

Figure 6.4: Distribution of energy deposited by annihilation gamma quanta at central position obtained from left E_L and right E_R photomultiplier in the range 0.2 to 0.38 MeV. Reason to select only the mentioned energy region is to avoid the energy produced by: secondary or multi Compton scattering, high energy gamma quanta which produced during the decay of ^{22}Na and also cosmic rays.

6.1.2.1 Bisection of energy region

In order to suppress the uncertainties arising due to the variation of time resolution as a function of number of photoelectrons, an energy loss region from 0.2 to 0.38 MeV was divided into two parts (R1 and R2). Energy regions lie in the divided parts were defined by the line drawn perpendicular to the diagonal (which follows the straight line equation y = x) of the distribution with the condition imposed on the energy loss by the signals:

- R1 consists of only those events for which $(E_L + E_R) < 0.58$ MeV
- R2 consists of only those events for which $(E_L + E_R) \geqslant 0.58$ MeV

where, E_L and E_R are the deposited energies reconstructed from left and right signals of an event, respectively. Bisected parts are shown in Fig. 6.5. Then, for each part, library of

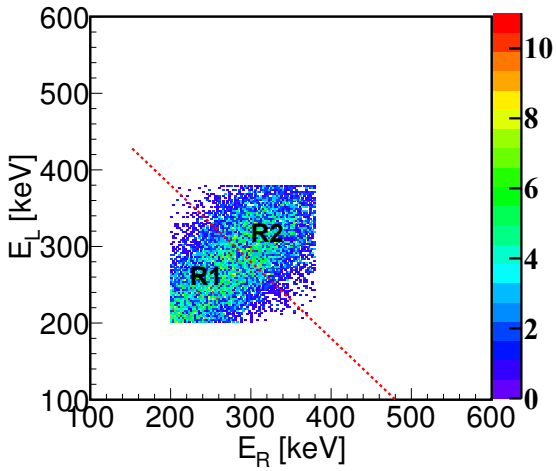

Figure 6.5: Bisection of energy loss region shown in Fig.6.4 into 2 parts (R1 and R2). Red dotted line is the line drawn perpendicular to the diagonal (which follow the straight line equation y = x). R1 is the region lying below the red dotted line and R2 is the region lying above the red dotted line.

model events and covariance matrix were computed separately as explained in Chapter 5. Next TOF distribution was calculated using [M.D(z, Δt)] (defined in Eq.5.5) separately for each part. Time-of-flight resolution obtained for each part is listed in Tab.6.3. For R1 TOF remained the same as it was obtained in section 6.1.1.2 but for R2 it has improved from 154 ps to 124 ps.

Table 6.3: Value of time-of-flight obtained for R1 and R2 parts (see Fig.6.5).

Region	rms(TOF error) [ns]
R1	0.155 ± 0.003
R2	0.124 ± 0.002

6.1.2.2 Multisection of energy region into four parts

From Tab.6.3 it is clear that resolution depends on deposited energy of signals. So, a test with next bisection of the plot shown in Fig.6.4 was also performed. Instead of two parts (R1 , R2) energy distribution was divided into four parts shown in Fig.6.6.

In Tab.6.4 results of best distribution of TOF among all sub-regions obtained at central hit-position are represented. It has been found that with further sub-division of energy distribution from 2 to 4 regions there is no significant improvement in the resolution.

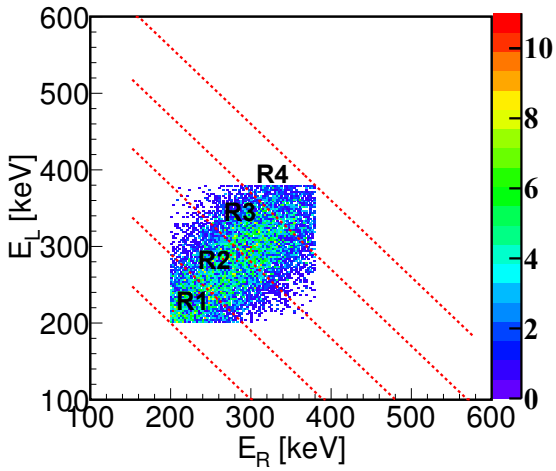

Figure 6.6: Division of energy loss region shown in Fig.6.4 into 4 different parts R1, R2, R3 and R4. Red dotted lines are the perpendiculars drawn on the diagonal of the distribution. **R1** composed of those events for which (E_L + E_R) < 0.49 MeV. **R2** part consisted of those events whose energy 0.49 ⩽ (E_L + E_R) < 0.58 MeV. Events with energy 0.58 ⩽ (E_L + E_R) < 0.67 MeV are lying in **R3**. Last part **R4** composed of those events for which (E_L + E_R) > 0.67 MeV.

Table 6.4: Value of time-of-flight obtained for R2 and R3 parts (see Fig.6.6).

Region	rms(TOF error) [ns]
R2	0.150 ± 0.004
R3	0.125 ± 0.004

6.1.3 Optimization of number of parameters in Mahalanobis distance

After optimizing the threshold level and deposited energy region next step was to optimize the number of free parameters used in the calculation of Mahalanobis distance. This was done by including charge (q) as the third parameter in the calculation of Mahalanobis distance. Now, Mahalanobis distance is a function of three parameters: hit-position (z), time shift (Δt) and charge (q). The reason to include charge in Mahalanobis formula is the dependency of signal's charge on hit-position. The addition of charge as another parameter leads to the addition of new row and column to the covariance matrix defined in section 5.3.2.2. Now, covariance matrix has $(m + 1)^2$ number of elements. In case of $\vec{x}$ defined in section 5.3.2.1 number of elements changed to (m + 1) instead of (m).

So, now covariance matrix and $\vec{x}$ for single threshold level became:

$$cov\ \ matrix[(z, \Delta t, q)] = \begin{bmatrix} a_{11} & a_{12} & a_{13} \\ a_{21} & a_{22} & a_{23} \\ a_{31} & a_{32} & a_{33} \end{bmatrix}$$

where,a_{11}, a_{12}, a_{21} and a_{22} are calculated with same formula as explained in section 5.3.2.2, where,

$$a_{13} = \sum_{k=1}^{N} \frac{[(t_L - t_{avg_L})(\frac{q_L}{q_R} - \frac{q_{avg_L}}{q_{avg_R}})]_k}{N} \ ,$$

$$a_{23} = \sum_{k=1}^{N} \frac{[(t_R - t_{avg_R})(\frac{q_L}{q_R} - \frac{q_{avg_L}}{q_{avg_R}})]_k}{N} \ ,$$

$$a_{33} = \sum_{k=1}^{N} \frac{[(\frac{q_L}{q_R} - \frac{q_{avg_L}}{q_{avg_R}})^2]_k}{N} \ ,$$

$$a_{31} = a_{13} \ ,$$

$$a_{32} = a_{23} \ ,$$

$$\vec{x}_k(z, \Delta t, q) = [x_1,\ x_2,\ x_3]_k$$

where, x_1 and x_2 were calculated in the same way as mentioned in section 5.3.2.1 and x_3 is defined as:

$$x_3 = \frac{q_L}{q_R} - \frac{q_{model_L}}{q_{model_R}}$$

where q_L, q_R denotes charge carried by left and right measured signals and q_{model_L}, q_{model_R} left and right model signals, respectively. The x_3 was defined as a ratio between charges of signals measured at the left and right side of the scintillator because this ratio carry the information about the position of gamma quanta interaction in the scintillator. For testing the effect of charge on the obtained resolution, the test was performed in the case when signals were distinguished on the basis of energy criteria mentioned in section 6.1.2.1. It was noticed that resolution deteriorate by including charge as another parameter in the formulation of Mahalanobis distance.

Hence, the dependence of Mahalanobis on charge will not be taken into account and the reconstruction of image will be performed on the two-threshold levels followed by the determination of covariance matrices separately for two energy regions: R1 with (E_L + E_R) $<$ 0.58 MeV and R2 with (E_L + E_R) $\geqslant$ 0.58 MeV using Mahalanobis distance as a function of z and Δt.

6.2 Optimization of signals processing from two strips module with dimensions 7x19x500 mm^3

For the J-PET two strip module built from scintillators with dimensions of 5x19x300 mm^3, the value of optimized two-threshold level was -55 mV and -100 mV (as discussed in section 6.1.1). However, for other J-PET module built by using scintillators with dimensions of 7x19x500 mm^3, the value of optimized two-threshold level can be different.

6.2.1 Optimized two-threshold level

The test was performed for signals measured at the center of the scintillator. Different combinations of thresholds were tested which are listed in Tab.6.5. Fig.6.7 represents the rms(TOF error) obtained at various combinations of thresholds.

Table 6.5: Combinations of two-level threshold applied to the measured signals.

S.No.	Levels [mV]
1	-50, -80
2	-50, -100
3	-55, -80
4	-55, -100
5	-60, -80
6	-60, -120
7	-60, -140
8	-60, -160
9	-80, -100
10	-80, -120
11	-80, -140
12	-80, -160
13	-100, -120
14	-100, -140
15	-100, -160
16	-120, -140
17	-120, -160

It is clear from Fig.6.7 that the values of rms(TOF error) for different combinations listed in Tab.6.5 are the same within the uncertainties. So, -60 and -80 mV were chosen as the optimum two-threshold level for two strips module with dimensions 7x19x500 mm^3.

6.2.2 Optimized energy distribution

It is evident from section 6.1.2 that there is no significant improvement in the resolutions by dividing the energy distribution from 0.2 MeV to 0.38 MeV into more than two regions.

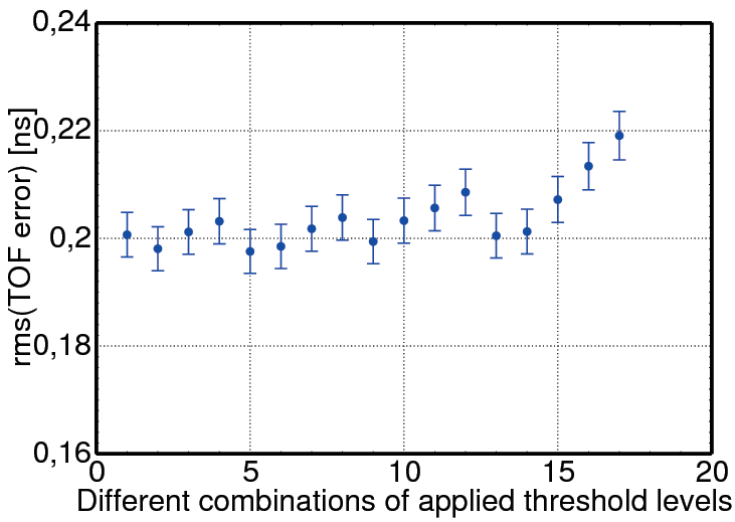

Figure 6.7: Distribution of rms (TOF error) for different combination of two threshold levels. On X-axis serial number of applied threshold values (listed in Tab.6.5) are mentioned

Hence, for the image reconstruction from the data measured by 7x19x500 mm^3 strips signal's were distinguished on the basis of their energy deposited in regions R1 and R2. Obtained values of TOF resolutions for these two regions are listed in Tab.6.6.

Table 6.6: Value of time-of-flight obtained for R1 and R2 regions (see Fig.6.5).

Region	rms(TOF error) [ns]
R1	0.189 ± 0.007
R2	0.159 ± 0.007

So far, the optimization of the threshold values and energy criteria were based on the comparison of signals using Mahalanobis distance. In the next section we will introduce an alternative method where the time of the signals is estimated by fitting a line at their leading edges.

6.3 Multi-threshold Technique

In this method the leading edge of a signal was sampled at a number of pre-defined voltage levels. After obtaining the digital samples, a line was fitted to them and the event time was estimated as the intercept of this line with the zero-voltage level as shown in Fig.6.8.

The method was implemented on the data collected from the two-strip J-PET module with dimensions of 5x19x300 mm^3 irradiated by collimated beam at the center of the scintillator. The test was performed with different number of threshold levels e.g. two-threshold levels, three-threshold levels and so on. For each number of levels different values

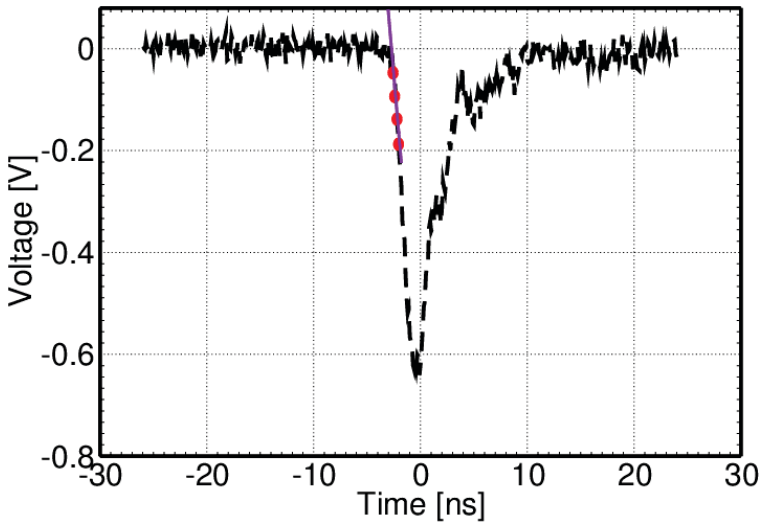

Figure 6.8: The multi-voltage threshold (MVT) method applied to a sample event pulse. The event time is defined by the intercept of the line fitted to the pulse's leading edge. Red circles indicate crossing of signals at applied threshold levels. Violet solid line is the line fitted to signal's leading edge passing through the applied threshold levels.

of threshold were tested. In Tab. 6.7 only those values for each number of applied levels are given for which we obtained best TOF resolution.

Table 6.7: Number of applied threshold levels with their values used in multi-voltage threshold method.

Number of applied levels	Values [mV]
2	-40, -80
3	-40, -80 , -120
4	-40, -80 , -120, -160
5	-40, -80 , -120, -160, -200
6	-40, -80 , -120, -160, -200, -240
7	-40, -80 , -120. -160, -200, -240, 280

Dependence of TOF resolution on the number of applied threshold levels is shown in Fig. 6.9. From this figure one can infer that : i) In general the TOF resolution is improving with the increase of the number of applied thresholds, ii) there is no significant improvement in rms(TOF error) for more than five thresholds levels, iii) obtained value of rms(TOF error) with six pre-defined threshold levels is comparable with value calculated using Mahalanobis method at two pre-defined threshold levels.

Although the algorithm of MVT technique is much easier than the algorithm of Mahalanobis method, but the realization of MVT technique is impractical because it requires six samples (six thresholds) to achieve the same resolution as achievable with two thresholds when applying method based on the Mahalanobis distance. More number of applied threshold levels would increase the cost of electronics used in the PET scanner, hence, it

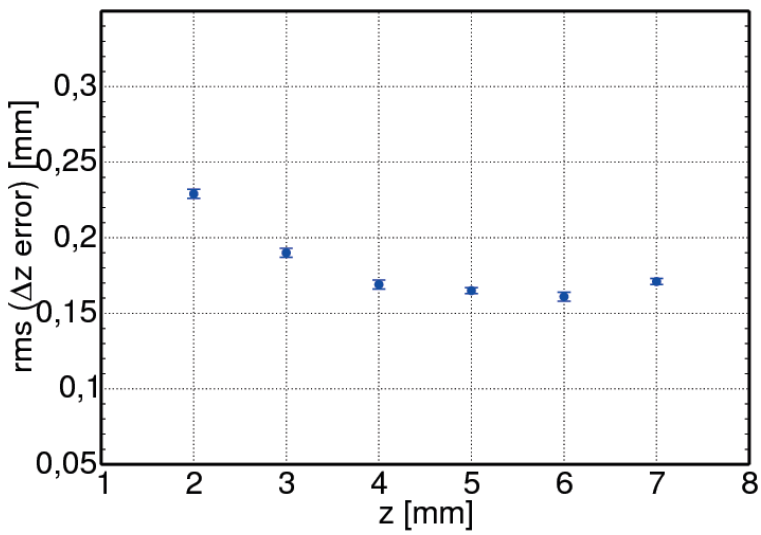

Figure 6.9: Dependence of the TOF resolution on the number of applied threshold levels obtained by multi-voltage threshold method. Values of applied threshold levels at each number is mentioned in Tab. 6.7.

would make it more expensive. Therefore, the Mahalanobis distance will be used for the reconstruction of hit-time and hit-position for each detector strip.

Chapter 7

2D Image reconstruction

Image reconstruction in PET delivers the distribution of radio-tracer in a patient′s body and 2D reconstruction is a particular subproblem of generalized 3D PET scanner. In the 2D reconstruction, a double strip module was considered as two parallel line segments of length L with a negligible thickness and separated by a distance 2R as it is shown in Fig. 7.1. The reconstruction is done iteratively using the list-mode version of maximum likeli-

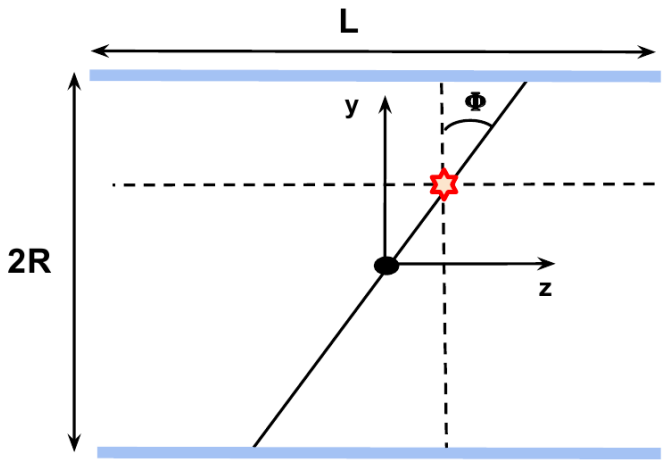

Figure 7.1: A schematic view of the double-strip J-PET prototype.

hood expectation maximization (MLEM) algorithm [64]. Each iteration of this algorithm is defined by

$$\rho(i)^{t+1} = \sum_{\tilde{e}\in\tilde{E}} \frac{P(\tilde{e}|i)\rho(i)^{(t)}}{\sum\limits_{j\in\nu} P(\tilde{e}|j)s(j)\rho(j)^{(t)}} \qquad for \quad i \in \mathrm{I} \tag{7.1}$$

where, t denotes number of iterations, i enumerates pixels in the image. $\rho(i)$ refers to the emission density, $\mathrm{P}(\tilde{e}|i)$ is the reconstruction kernel which represents the probability that detected event $\tilde{e}$ originates from the pixel i and $s(i)$ is the *sensitivity* of the pixel i [64]. $\mathrm{P}(\tilde{e}|i)$ is defined by Eq. 7.2 and $s(i)$ for image point $(y,\ z)$ is given by Eq.7.3. Eq. 7.2 and Eq.7.3 have been derived by using several approximations mentioned in [64].

Validation of the used approximations has been checked by Monte-Carlo simulations of 2D strip detector response to a point source at three different (z,y) positions: (0,0) cm, (10, 0) cm and (10, 10) cm and the results are presented in [64].

$$P(\tilde{e}|i) = \frac{P(\tilde{e} \cap i)}{s(i)} \tag{7.2}$$

$$s(i) = \int\limits_{y,z \in i} s(y,z) \tag{7.3}$$

where, $s(y,\ z)$ the sensitivity for image point $(y,\ z)$. $s(y,\ z)$ includes geometrical acceptance and detection efficiency of the tomograph for the registration of annihilations occurring in point $(y,\ z)$ [64] and it is further expressed as:

$$s(y,z) = \pi^{-1} \int\limits_{-\pi/2}^{\pi/2} d\phi s(y,z,\phi) \tag{7.4}$$

7.1 Spatial resolution

In NEMA NU-2 [65] standard published by *National Electrical Manufacturers Association* (NEMA) the performance measures of PET scanners were proposed. Spatial resolution is one of them. Measuring the response of an imaging system to a high-contrast point-like source distribution is known as point spread function PSF. In case of PET, PSF is the three-dimensional image of PET scanner's response to a point-like emitting object (phantom). Point spread function (PSF) is defined as a full width at half maximum (FWHM) of the image of ^{18}F source with dimensions of 1 mm. PSF depends on the position of the source inside the diagnostic chamber. Therefore, six representative positions are defined in the NEMA norm for which the PSF has to be established. These six positions are as follows:

In axial direction: At the center and at a distance of three-eights of the center of axial field-of-view (FOV) along the planes.

In transverse direction: The source shall be positioned at 1 cm, 10 cm and 20 cm from the center of the plane on either horizontal or vertical line intersecting the system axis in order to have an alignment of radial and tangential directions with the image grid.

It is possible to simulate a virtual phantom with point's zero-dimensions and a non-zero emission intensity, but in real life it is not possible. A physical phantom must have non-zero dimensions in order to reach desired emission intensity.

Chapter 8

Results

8.1 J-PET prototype of two 5x19x300 mm^3 strips

The measurements with the double strip setup were performed in three steps:

- **Measurements with collimated beam**

Scan of whole strips along their length was done by irradiating with a collimated beam (FWHM ∼1.5 mm) of annihilation quanta produced by ^{22}Na with a step of 3 mm using a dedicated mechanical system and a step-motor which allowed the collimator to move along Z-axis with a precision of a fraction of millimeter. General scheme of experimental setup is shown in Fig.4.1. For 5x19x300 mm^3 strips the first, central and last irradiated positions (z, y) were (-150, 0) mm , (0, 0) mm and (150, 0) mm, respectively. An exemplary time-of-flight and spatial (Δz) distributions at optimized two-threshold levels with values -55 mV and -100 mV followed by the determination of covariance matrices separately for energy loss lying in regions R1 and R2 (mentioned in Chapter 6) are shown in Fig.8.1. For each region R1 or R2 their respective standard libraries signals were used. The mean of the distributions presented in Fig.8.1(a) and Fig.8.1(b) is not zero but shifted by ∼6 ns. The reason of this offset is the time delay because of the difference in the length of cables used to readout the output from the PMs connected to the ends of the scintillator and it was the same for all the hit-positions along the length of scintillator. The time-of-flight and spatial resolutions for the hit-positions in the range from (-100, 0) mm to (100, 0) mm along the length of scintillator are presented in Fig.8.2. For the hit-positions closer to the edge of the scintillator the statistics to be used to reconstruct the hit-positions and hit-time using Mahalanobis distance were very low. For events in which gamma quanta hit in the proximity of edge of the scintillator, there is a possibility that the one of the signal from the same event does not qualify the selection criterion based on energy deposition and hence is discarded. Furthermore, for the TOF calculation it is necessary to have two events registered in two strips from the same annihilation point of gamma quanta and because of selection criterion the possibility to have such events get reduced and hence the obtained statistics were insufficient to reconstruct the hit-position and hit-time.

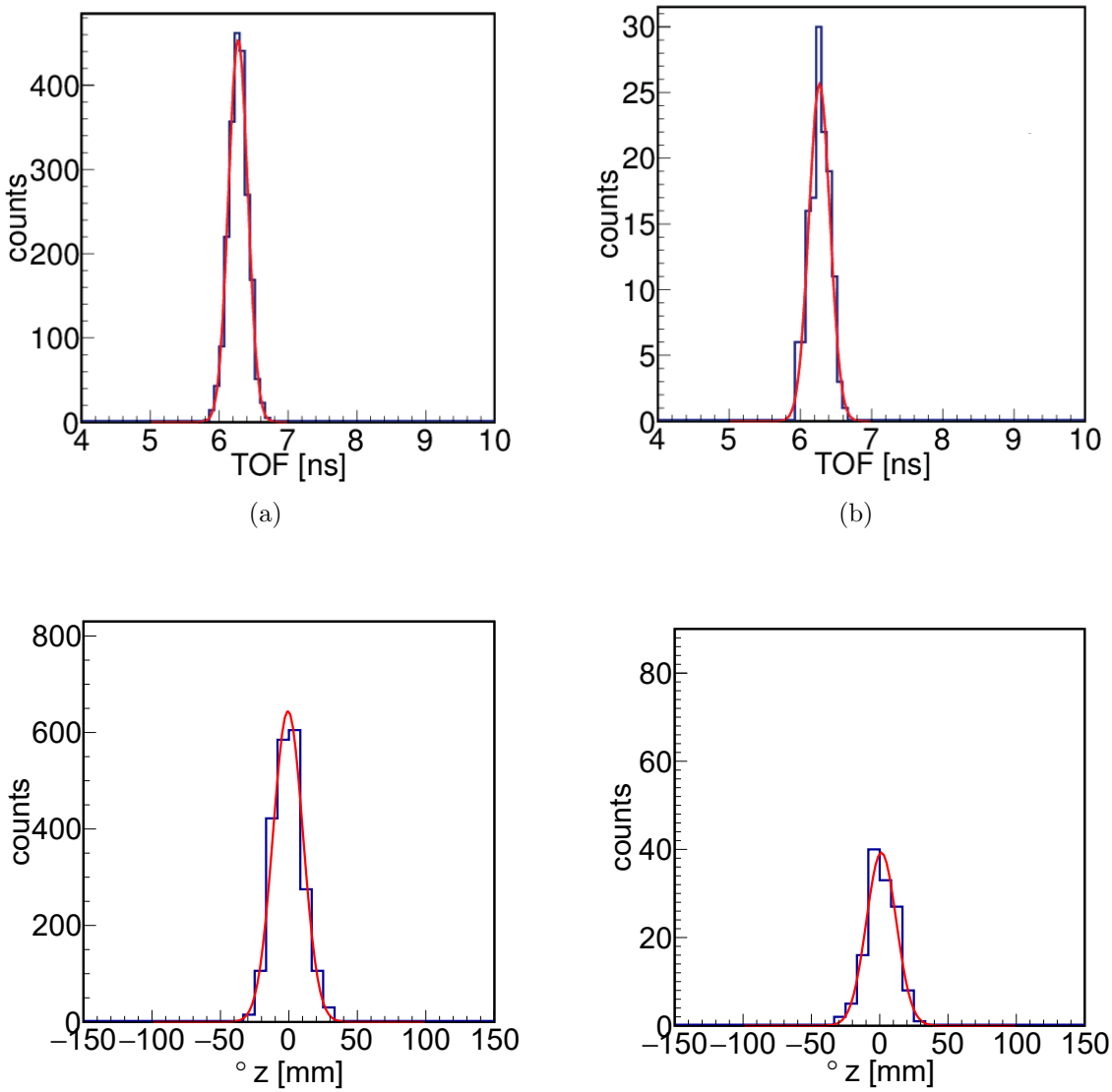

Figure 8.1: TOF and spatial (Δz) distributions: (a) TOF distribution at central hit-position with rms (TOF error)= 0.138 $\pm$ 0.002 ns. (b) TOF distribution for the hit-position closer to the edge of the scintillator with rms (TOF error)= 0.143 $\pm$ 0.003 ns. (c) Spatial (Δz) distribution at central hit-position with rms (Δz error)= 10.7 $\pm$ 0.2 mm. (d) Spatial (Δz) distribution for the hit-position closer to the edge of the scintillator with rms (Δz error)= 10.8 $\pm$ 0.67 mm.

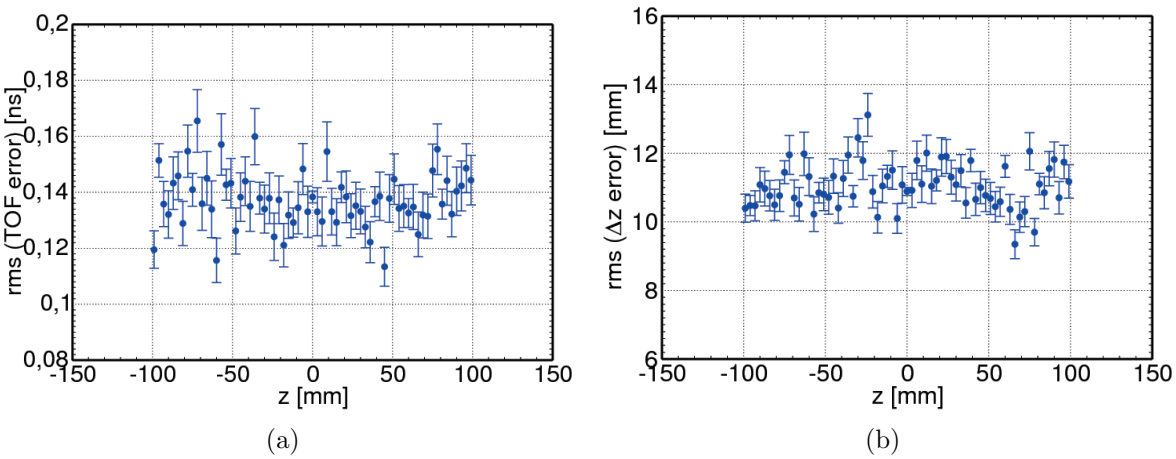

Figure 8.2: Resolutions as a function of the hit-position (z) for the plastic strips with dimensions 5x19x300 mm^3 along the detector at optimized two-threshold levels. (a) TOF resolution (b) Spatial (Δz) resolution.

- **Measurements with twisted collimated beam**

The measurements were performed by twisting the collimated beam, by an angle θ (15^0 and 30^0) in clockwise and anti-clockwise directions at the central hit-position of scintillator. The results are listed in Tab. 8.1 in terms of time-of-flight (TOF) resolution and spatial (Δz) resolution by comparing the measured events with each model event stored in the standard signal libraries (created by the scan measurement) using Mahalanobis distance as a measure of similarity at optimized two-threshold levels with values -55 mV and -100 mV followed by the determination of covariance matrices separately for energy deposition lying in regions R1 and R2 (mentioned in Chapter 6). For each region R1 or R2 their respective standard signal libraries were used.

Table 8.1: Time-of-flight (TOF) resolution and spatial resolution (Δz) at different angle of collimation .

Collimated angle	rms(TOF error) [ns]	rms(Δz error)[mm]
15^0 clockwise	0.135 ± 0.004	11.7 ± 0.4
15^0 anti-clockwise	0.129 ± 0.004	10.9 ± 0.4
30^0 clockwise	0.145 ± 0.004	12.2 ± 0.4
30^0 anti-clockwise	0.151 ± 0.005	10.2 ± 0.3

- **Measurements with non-collimated beam**

The measurements were performed with bare sources (i.e. unrestricted 4π directions of emission) placed in the 3x3 matrix module as shown in Fig.8.3 and the position of each slot marked in 3x3 matrix module with respect to the center of scintillator is presented in Fig.8.4. In Tab.8.2 used sources with their radioactivity are listed.

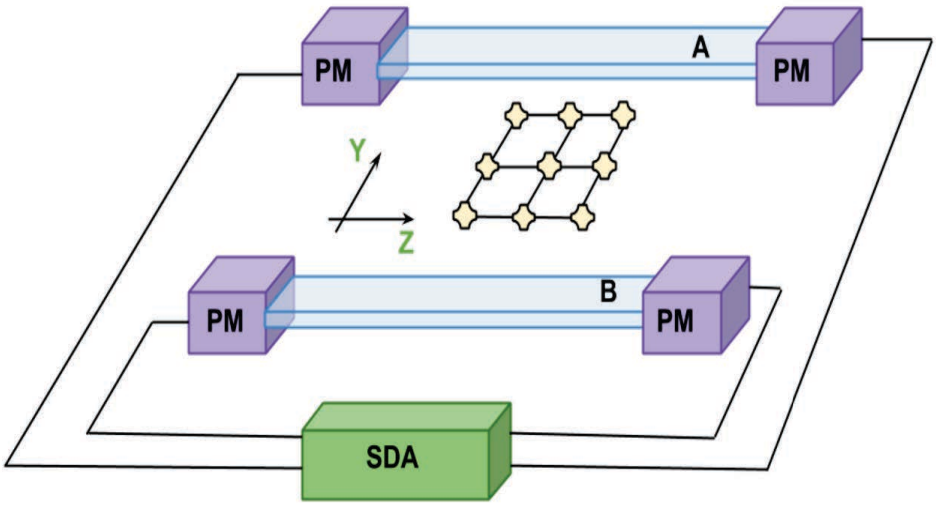

Figure 8.3: Experimental setup for source measurement. Both the scintillators were 41 cm apart from each other along Y-axis and from the position of source located at central position (i.e at (0, 1) see Fig.8.4) each of them are at a distance of 20.5 cm along Y-axis.

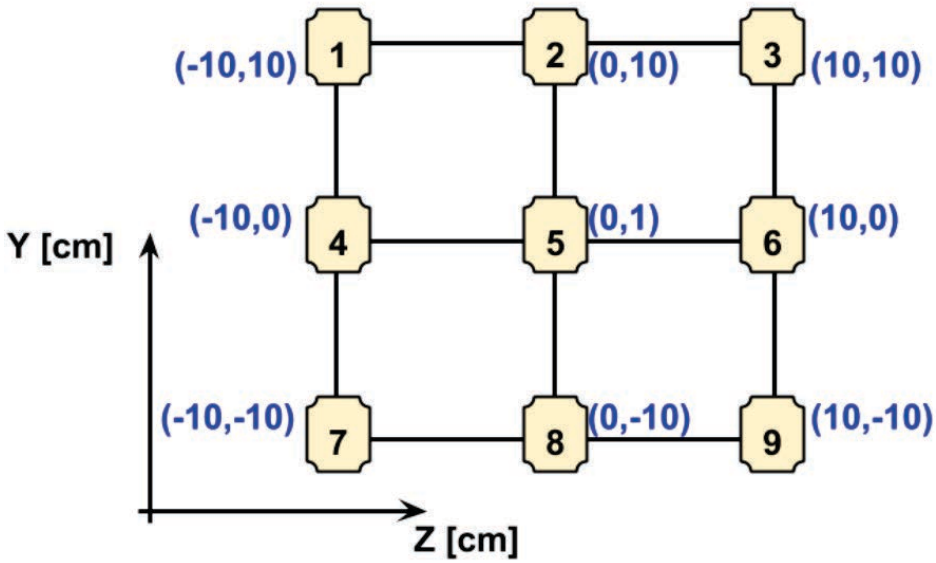

Figure 8.4: Positions of source within the matrix

Table 8.2: List of different ^{22}Na sources used for the source measurement.

Source No.	Activity [kBq]
37/12	393
07/11	140
39/12	399
38/12	391
UR451	2180
K4-390	11946
UR450	2185
105B	280
50/13	9

Measurement was done in four steps with different number of sources placed at different position of 3x3 matrix module marked in Fig. 8.4:

- *One source*: When only one source with label UR451 (from Tab.8.2) was used at each position marked in 3x3 matrix module Fig.8.4.
- *Two sources* : When two sources with labels UR450 & UR451 (see Tab.8.2) were used, the source UR451 was fixed at position 5 and the position of UR451 keep on changing from 1,2,3,4,6,7,8,9 as marked in 3x3 matrix module Fig.8.4.
- *Three sources*: When three sources with labels UR450, UR451 & 38/12+39/12 (glued with tape) were used at positions listed in Tab.8.3:

Table 8.3: Combinations of different positions used to place three sources .

Sources used	their positions in 3x3 matrix
UR450, UR451, (38/12+39/12)	1, 4, 7
UR450, UR451, (38/12+39/12)	2, 5, 8
UR450, UR451, (38/12+39/12)	3, 6, 9
UR450, UR451, (38/12+39/12)	1, 2, 3
UR450, UR451, (38/12+39/12)	4, 5, 6
UR450, UR451, (38/12+39/12)	7, 8, 9
UR450, UR451, (38/12+39/12)	1, 5, 9
UR450, UR451, (38/12+39/12)	3, 5, 7

- *Nine sources*: When all the marked positions of 3x3 matrix module Fig.8.4 were occupied by some source.

8.1.0.1 Spatial resolution

This section is dedicated to the determination of spatial resolution using MLEM reconstruction. This is done by providing the output file obtained from Mahalanobis distance

as a input to MLEM reconstruction. This output file have the information about the hit-positions and hit-times of all the events corresponding to each configuration of source. The hit-times ad hit-positions obtained as a result of comparison between the measured and each model event stored in standard signal libraries (created by scan measurement) at optimized two-threshold level with values -55 mV and -100 mV followed by the determination of covariance matrices separately for energy loss lying in regions R1 and R2 (mentioned in chapter 6). For each region R1 or R2 their respective standard signal libraries were used.

The PSF for the single source placed at position (0,1) is shown in Fig. 8.5 and the detailed images from different configuration of sources (Chapter 7) are shown in Fig.8.6 and the exemplary projections of image from Fig.8.6(a) are shown in Fig.8.7.

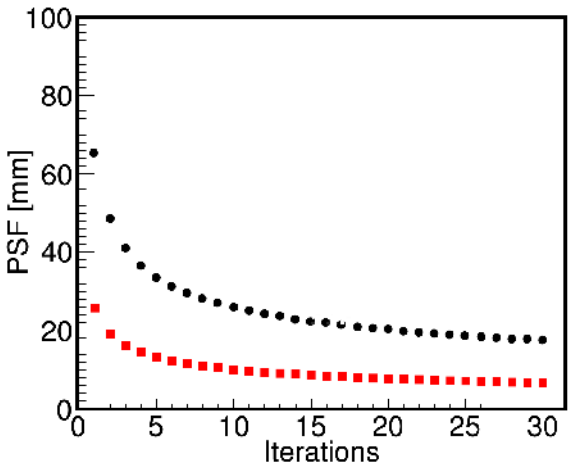

Figure 8.5: PSF determined at position (0, 1) cm for double strip J-PET prototype as a function of the number of iterations. Black circles represents the transversal PSF determined as a projection onto the Y-axis of the detector. Red squares denotes axial PSF determined as a projection onto the Z-axis of the detector.

From Fig.8.5 it is clear that after 20 iterations there is no further improvement in PSF. In Tab.8.4 the values of PSF in Y and Z axes when the source was placed at position (0, 1) closer to the central position and at position (10, 0 cm) (i.e. when it was 10 cm displaced from the central position) are shown.

Table 8.4: PSF at different positions of source (see Fig.8.4)

Source size (diameter)	Source position [cm]	Z_{PSF} at 20th iteration [mm]	Y_{PSF} at 20th iteration [mm]
less than 3 mm	[0, 1]	7.7	20.2
	[10, 0]	8.4	21.2

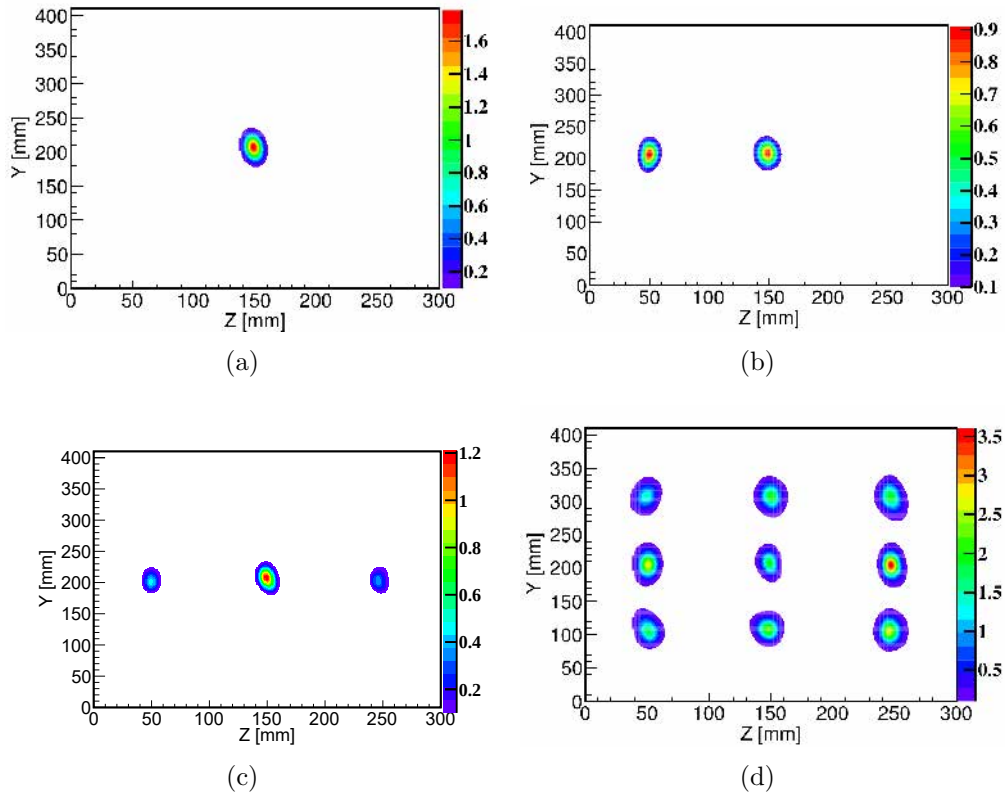

Figure 8.6: 2D image reconstructed for different configuration of sources in 3x3 matrix module using MLEM. Image of the source (a) placed at central position 5 (Tab.8.2), (b) sources placed at 4 and 5 positions, (c) sources placed at 4 ,5 and 6 positions, (d) sources placed at all the marked positions of 3x3 matrix module.

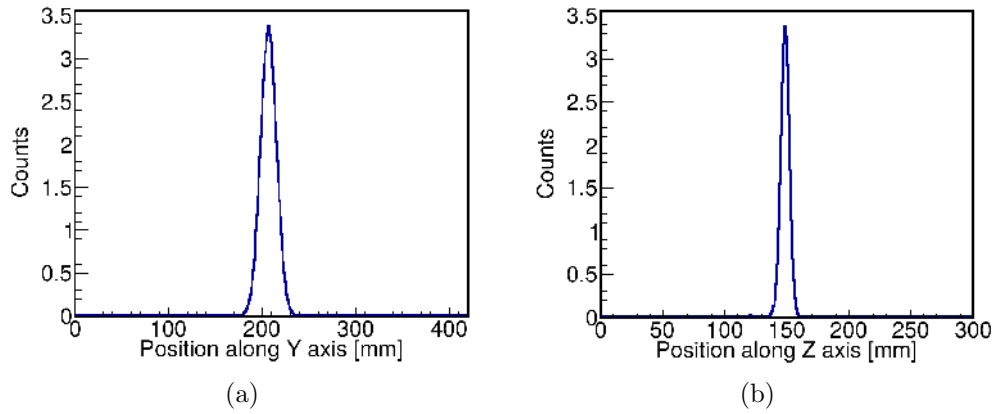

Figure 8.7: Projections of image from Fig.8.6(a) in Y and Z directions. (a) Projection along Y-axis (b) Projection along Z-axis.

8.2 J-PET prototype of two 7x19x500 mm^3 strips

This measurement was also done in three steps:

- **Measurements with collimated beam**

Scan of whole strips along their length was done as for previous case by irradiating them with a collimated beam (FWHM ∼1.5 mm) of annihilation quanta produced by ^{22}Na with its active part in the form of cylinder with diameter of 3 mm and thickness of 1 mm with a step of 3 mm using a dedicated mechanical system and a step-motor which allowed the collimator to move along Z-axis with a precision of a fraction of millimeter. General scheme of experimental setup is shown in Fig.4.1.

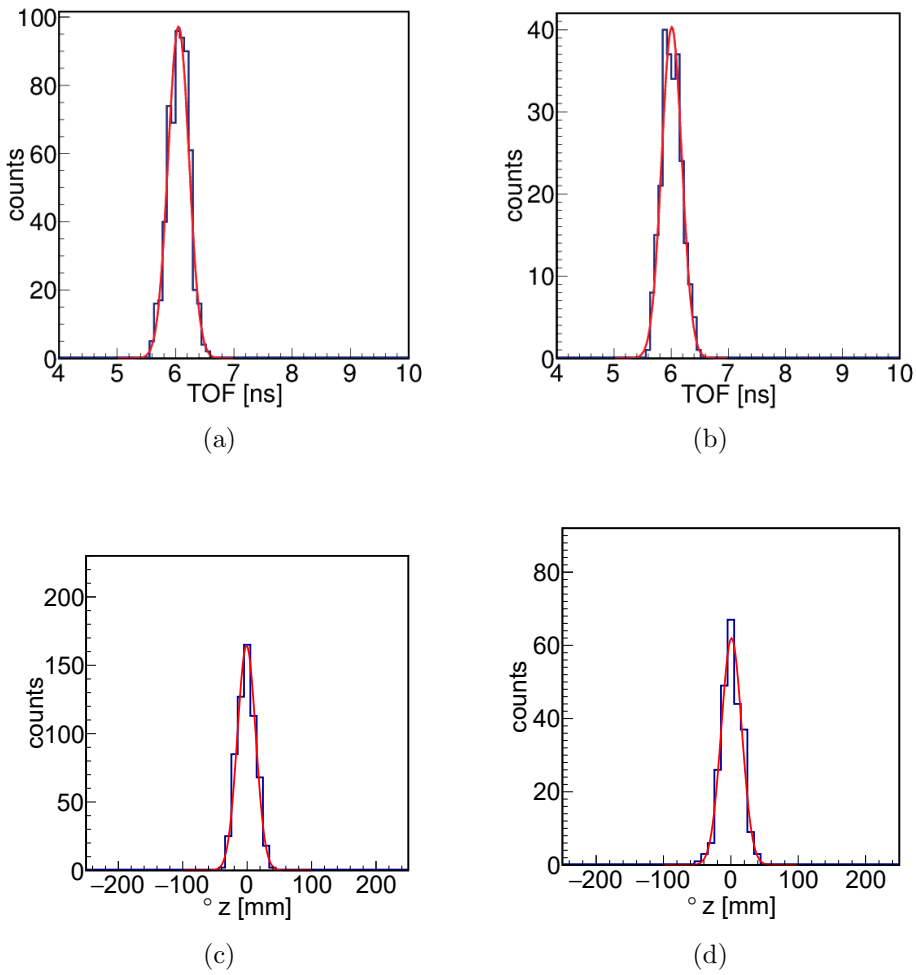

Figure 8.8: TOF and spatial (Δz) distributions: (a) TOF distribution at central hit-position with rms (TOF error)= 0.176 ± 0.005 ns. (b) TOF distribution for the hit-position closer to the edge of the scintillator with rms (TOF error)= 0.177 ± 0.007 ns. (c) Spatial (Δz) distribution at central hit-position with rms (Δz error)= 13.7 ±0.4 mm. (d) Spatial (Δz) distribution for the hit-position closer to the edge of the scintillator with rms (Δz error)= 15 ± 0.7 mm.

For 7x19x500 mm^3 strips the first, central and last irradiated positions (y, z) were (-220, 0) mm , (0, 0) mm and (221, 0) mm, respectively. An exemplary time-of-flight and

spatial (Δz distributions at optimized two-threshold levels with values -60 mV and -80 mV followed by the determination of covariance matrices separately for energy loss lying in regions R1 and R2 (mentioned in Chapter 6) are shown in Fig.8.8. For each region R1 or R2 their respective standard signal libraries were used. The time-of-flight and spatial resolutions of all hit-positions along the length of scintillator are presented in Fig.8.9.

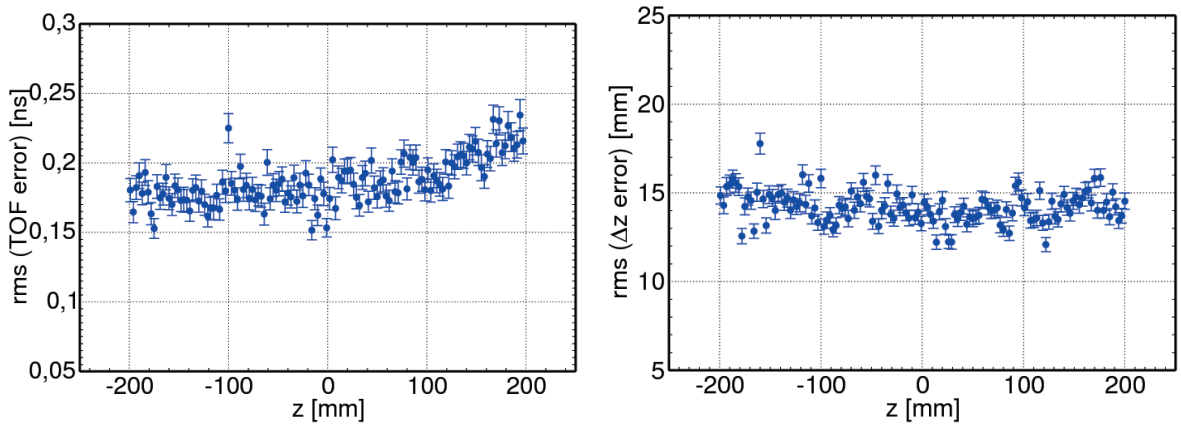

(a) (b)

Figure 8.9: (a) TOF resolution as a function of the hit-position (z) along the detector at optimized two-threshold levels with the division of deposited energy region into two: R1 and R2. (b) Spatial resolutions (Δz) as a function of the hit-position (z) along the detector at optimized two-threshold levels with the division of deposited energy region into two: R1 and R2 .

- **Measurements with twisted collimated beam**

As for previous case, the measurements were performed by twisting the collimated beam, with an angle θ (15^0 and 30^0) in clockwise and anti-clockwise directions at the central hit-position of scintillator. Tab.8.5 represents the results obtained in terms of time-of-flight (TOF) and spatial (Δz) resolutions.

Table 8.5: Time-of-flight resolution and spatial resolution (Δz) at different angle of collimation .

Collimated angle	rms(TOF error) [ns]	rms(Δz error)[mm]
15^0 clockwise	0.187 ± 0.005	14.1 ± 0.4
15^0 anti-clockwise	0.188 ± 0.005	15.0 ± 0.4
30^0 clockwise	0.184 ± 0.005	15.1 ± 0.4
30^0 anti-clockwise	0.198 ± 0.005	15.5 ± 0.4

- **Measurements with non-collimated beam**

The measurement was performed with two bare sources UR450 and UR451 (mentioned in Tab.8.2) positioned in two different configurations.

- when source UR451 was at position (0, 0) cm and source UR450 at (-2.6, 0) cm.
- when both the sources were displaced from their previous positions by 10 cm along Z-axis.

The analysis is done by providing the output file with the information of hit-positions and hit-times of all the events corresponding to each configuration of source as a input to MLEM (as described in section 8.1.0.1). But the optimum two-threshold level used for this set of data was -60 mV and -80 mV. Fig.8.10 represents the setup used for the measurements. Images reconstructed from different configuration of sources using MLEM are shown in Fig.8.11 and their zoom view is shown in Fig.8.12.

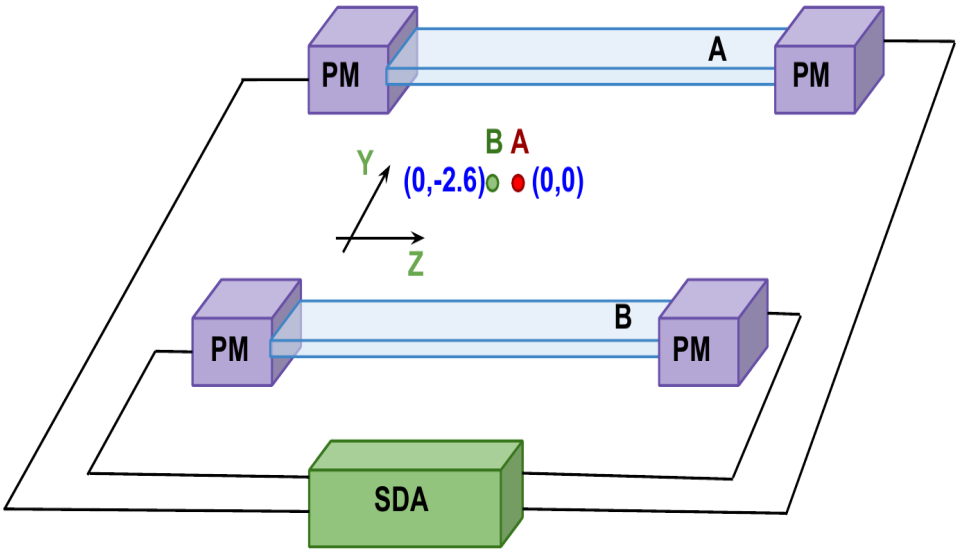

Figure 8.10: Scheme of experimental setup used in bare sources measurements. Both the scintillators were 41 cm apart from each other along Y-axis and from the position of source located at central position (i.e at (0, 0)) each of them are at a distance of 20.5 cm along Y-axis. Point **A** represents the position of source UR451 and **B** represents the position of source UR450. The centers of both sources were 2.6 cm apart from each other.

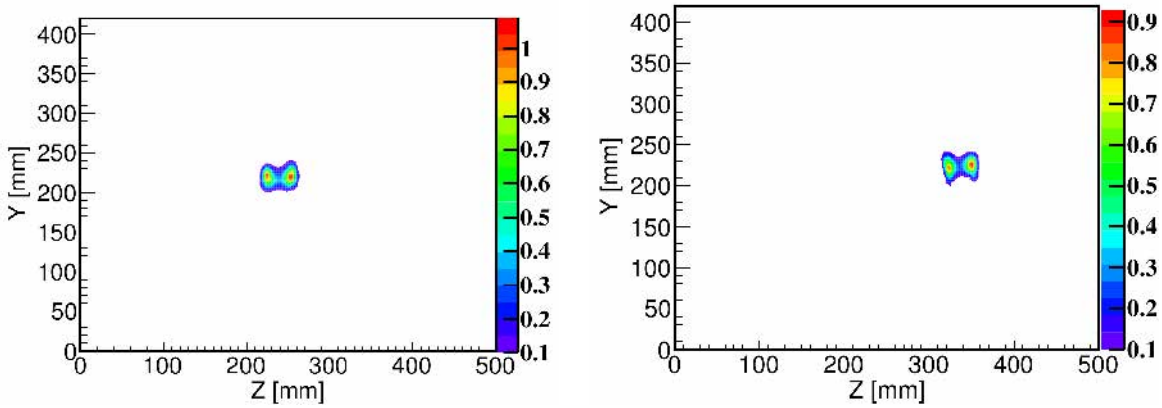

(a) (b)

Figure 8.11: 2D image reconstructed for different configuration of sources using MLEM. (a) Image reconstructed for sources placed at (0,0) cm and (-2.6, 0) cm positions. (b) Image reconstructed for sources placed at (10, 0) cm and (7.4, 0) cm.

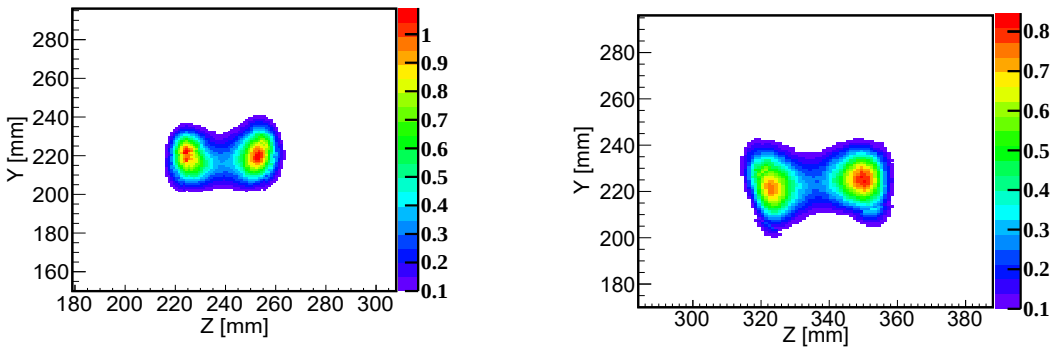

(a) (b)

Figure 8.12: Zoomed 2D image view for (a) sources placed at (0,0) cm and (-2.6, 0) cm positions. (b) sources placed at (10, 0) cm and (7.4, 0) cm.

Chapter 9

Summary and perspectives

The present work demonstrates the feasibility studies to use plastic scintillators as an alternative of crystal inorganic scintillators currently being used in commercial Positron Emission Tomography. Key parameters of commercial PET scanners and the J-PET prototype are listed in Tab.3.1.

Studies were carried out with the two-strip J-PET prototype focusing on various aspects of imaging properties. The main aim was to elaborate a method for the precise determination of hit-position and hit-time of gamma quanta in scintillator for producing the good quality tomographic images. In order to achieve this aim, an algorithm was developed which estimates the similarity between the registered signal and synchronized model signals. Mahalanobis metric was used as a measure of similarity. The method was optimized for number of threshold levels with different combinations, energy loss regions and number of parameters included to calculate the value of Mahalanobis distance. TOF resolution was the criterion of the optimization. As a result, it was found that best TOF resolution can be obtained from Mahalanobis distance when signals were processed at two-threshold levels with the division of energy deposition region from 0.2 MeV to 0.38 MeV into two parts: i) $(E_L + E_R) < 0.58$ MeV ii) $(E_L + E_R) \geqslant 0.58$ MeV. Furthermore, TOF resolution was also calculated from one more method named multi-threshold technique. With this method the best TOF resolution was obtained at six pre-defined threshold levels which was comparable to the resolution achieved from Mahalanobis distance at two pre-defined threshold levels. Thus, as regards, time and position resolution, the optimum J-PET design should include two threshold readout. Further increase of number of thresholds increases costs and complexity but does not improve the resolution significantly.

Obtained values of the hit-time and hit-position from Mahalanobis distance were used to reconstruct a 2D image by applying the Maximum Likelihood Expectation Maximization (MLEM) method. Resolution for various parameters in imaging field obtained from two-strip studies were listed and compared with commercial PETs in Tab.9.1

Table 9.1: Comparison between the resolutions of commercial PET scanners [1] [2] and the J-PET two-strip prototype

	Philips (Ingenuity TF)	GE (Discovery 710)	Siemens (Biograph mCT Flow)	Philips (Vereos)	J-PET two-strip prototype 5x19x300 mm^3 / 7x19x500 mm^3
Scintillator size (mm^3)	4x4x22	4.2x6.3x25	4x4x20	4x4x22	5x19x300/7x19x500
TOF resolution (ps)	550	544	540	345	325/414
TOF localization (cm)	8.9	8.2	8.1	5.2	4.9/6.2
Axial resolution @ 1 cm (mm)	4.7	5.6	4.5	4.0	7.7/ -
Axial resolution @ 10 cm (mm)	5.2	6.3	5.9	4.5	8.4/ -
Transaxial resolution @ 1 cm (mm)	4.7	4.9	4.4	4.0	20.2/ -
Transaxial resolution @ 10 cm (mm)	5.2	5.5	4.9	4.5	21.2 / -

From Tab.9.1 it is clear that image reconstructed with the J-PET two strip prototupe has comparable resolutions in terms of time-of-flight (TOF) and TOF localization to the one obtained from commercial tomographs. The axial and the transaxial resolutions are worse in comparison to commercial tomographs and need to be improved. In the two strip J-PET prototype we used only a pair of scintillators and that is why it has large uncertainty in localization of annihilation point (especially in transaxial direction). This can be improved in the J-PET full frame prototype built out of 192 scintillators positioned along a cylindrical geometry in 3 layers forming a 3D geometry with a FOV of about 85 cm and axial length of about 50 cm [55]. With the arrangement of scintillators (shown in Fig.9.1) in 3D geometry the uncertainty in localization of annihilation point in transaxial direction will be largely reduced as one will have more LOR's measured by many independent pairs of scintillators positioned at various Y-positions. Furthermore, more number of layers will also increase the detection efficiency.

Wavelength-shifters (WLS) can also be used for further improvement of axial resolution [66]. They will help in registering photons leaving the scintillator strip. The photons

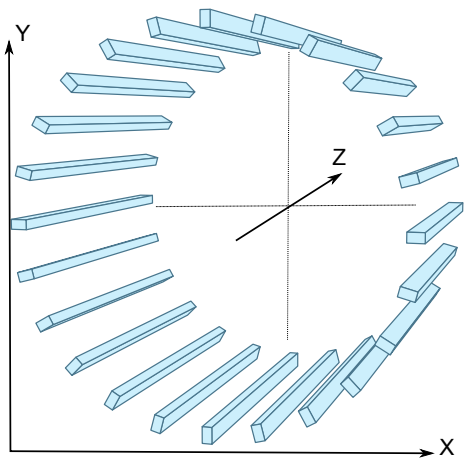

Figure 9.1: Pictorial representation of scintillators with dimensions 7x19x500 mm^3 arranged in the inner layer of the J-PET full frame prototype.

which reach the WLS array are emitted in the scintillator within two identical cones: forward and backward, with an angle equal to the twice of the critical angle in the scintillator material [66]. The photons which were emitted within the backward cone can be reflected back to WLS strips using a specular foil as it is illustrated in Fig.9.2. The distribution of signals amplitudes registered with WLS strips enable to determine the hit-position along the strip with the precision of 5mm [66]

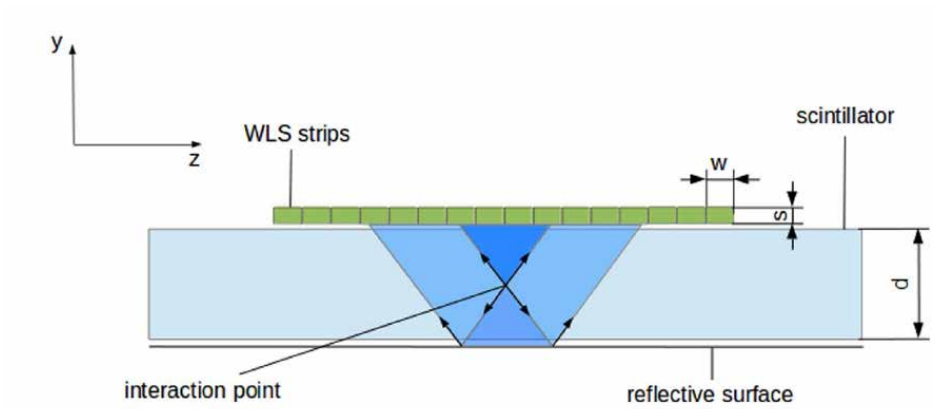

Figure 9.2: Principle of measuring axial coordinate of annihilation point in the scintillator using wavelength-shifter (WLS)'s array [66].

The use of the algorithm developed in this work to find the hit-time and hit-position of gamma quanta in the framework of the full J-PET prototype might provide comparable resolutions to commercial PETs not only for TOF but also for axial spatial coordinates properties providing a cost competitive positron emission tomograph.

Bibliography

[1] S. Vandenberghe et al., *Recent developments in time-of-flight PET,* EJNMMI Physics **3** 2016 1-30.

[2] P. J. Slomka et al., *Recent Advances and Future Progress in PET Instrumentation,* Sem. Nucl. Med. **46(1)** (2016) 5.

[3] P. Moskal, *Patents granted in 2014*, Nos. EP2454612, WO2011008119, US8859973, EP2454611, WO2011008118, US8969817.

[4] Saint Gobain Crystals, http://www.crystals.saint-gobain.com.

[5] Scinox organic scintillators, http://scionix.nl/frame/

[6] M. Battaglieri, *Scintillation Detetctors,* https://www.ge.infn.it/∼batta/Lect1-scint.pdf.

[7] R. Mao, L. Zhang, R. Y. Zhu, *Optical and scintillation properties of inorganic scintillators in high energy physics,* IEEE Nuclear Science Symposium Conference Record **N49** (2007).

[8] P. Moskal ,..N. G. Sharma, et al.,*Time resolution of the plastic scintillator strips with matrix photomultiplier readout for JPET tomograph,* Phys. Med. Biol., **61** (2016) 2025.

[9] J. S. Karp, S. Surti, M.E. Daube-Witherspoon, G. Muehllehner, *Benefit of Time-of-Flight in PET: Experimental and Clinical Results,* J Nucl. Med. **49** (2008) 462.

[10] P. Moskal et al., *Novel detector systems for the Positron Emission Tomography,* Bio-Algorithms and Med-Systems **7** (2011) 73.

[11] P. Moskal et al., *Strip-PET: A novel detector concept for the TOF-PET scanner,* Nuclear Medicine Review, **15** (2012) C68.

[12] P. Moskal et al., *TOF-PET detector concept based on organic scintillators,* Nuclear Medicine Review **15** (2012) C81. [arXiv:1305.5559[physics.ins-det]].

[13] L. Raczyński,..,N. G. Sharma, et al.*Novel method for hit-positon reconstruction using voltage signals in plastic scintillators and its application to the Positron Emission Tomography,* Nucl. Instrum. and Meth., **A764** (2014) 186.

[14] L. Raczyński,..,N. G. Sharma, et al., *Compressive sensing of signals generated in plastic scintillators in a novel J-PET instrument,* Nucl. Instrum. and Meth., **A786** (2015) 105.

[15] P. Moskal,..,N. G. Sharma, et al., *A novel method for the line-of-response and time-of-flight reconstruction in TOF-PET detectors based on a library of synchronized model signals,* Nucl. Instrum. and Meth., **A775** (2015) 54.

[16] N. Zoń, *Reconstruction of hit-position of gamma quanta in scintillators based on sampling of signals in voltage and fraction domains,* Diploma dissertation (2014).

[17] P. C. Mahalanobis, *On the generalised distance in statistics,* Proceedings of the National Institute of Science of India **2** (1936) 49.

[18] P.Moskal, N. G. Sharma.., et al., *Hit-time and hit-position reconstruction in the J-PET detector based on library of averaged model signals,* Acta Phys. Polon. A, **127** (2015) 1495.

[19] N. G. Sharma, et al., *Reconstruction of hit-time and hit-position of annihilation quanta in the J-PET detector using Mahalanobis method,* Nukleonika, **60** (2015) 765.

[20] M. Pałka,..,N. G. Sharma, et al., *A novel method based solely on FPGA units enabling measurement of time and charge of analog signals in Positron Emission Tomography,* Bio-Algorithm and Med-System **10** (2014) 41.

[21] Principle of PET, *https://www.tudelft.nl/en/faculty-of-applied-sciences/about-faculty/departments/radiation-science-technology/denkova-group/research/tof-pet/.*

[22] Robley D. Evans, *Text book the atomic,* Tata McGraw-Hill Publishing Company LTD Bombay-New delhi, (1955).

[23] G.F. Knoll, *Radiation Detection and Measurement* John Wiley & Sons, New York, **3rd edition** (2000).

[24] Interaction of gamma via photoelectric effect, *https://www.nuclear-power.net/nuclear-power/reactor-physics/interaction-radiation-matter/interaction-gamma-radiation-matter/photoelectric-effect/.*

[25] S. N. Ahmed, *Physics and Engineering of Radiation Detection,* Academic Press, Elsevier, **20** (2007).

[26] Interaction of gamma via pair-production , *https://www.electrons.wikidot.com/pair-production-and- annihilation/.*

[27] C. L . Melcher, *Scintillation Crystals for PET,* J. Nucl. Med. **6** (2000) 41.

[28] W. R. Leo, *Techniques for Nuclear and Particle Physics Experiments: A How to Approach,* **2nd edition** (1992).

[29] A. Wieczorek, *Development of novel plastic scintillators based on polyvinyltoluene for the hybrid J - PET/MR tomograph,* Ph.D dissertation, (2017).

[30] S. Surti, J. Karp, G. Muehllehner, P. Raby, *Investigation of Lanthanum scintillators for 3-D PET,* IEEE Trans Nucl Sci. **50** (2003) 348.

[31] P. Dorenbos, *Light output and energy resolution of Ce3+-doped scintillators,* Nucl Instrum Methods Phys Res A. **486** (2002) 208.

[32] P. Dorenbos, J. de Haas , C. van Eijk, *Non-proportionality in the scintillation response and the energy resolution obtainable with scintillation crystals,* IEEE Trans Nucl Sci. **42** (1995) 190.

[33] C. Kuntner, H. Aiginger, E. Auffray, J. Glodo, M. Kapusta, P. Lecoq ,M. Moszynski , M. Schneegans , P. Szupryczynski , AJ. Wojtowicz, *Scintillation properties and mechanism in Lu0:8Y0:2AlO3:Ce,* Nucl Instrum Methods Phys Res A. **486** (2002) 176.

[34] Hamamatsu Handbook, *Photomultiplier Tubes Basics and Applications,* Hamamatsu Photonics K.K., Electron Tube Division, **3rd edition** (2007).

[35] P.E. Valk, D.L. Bailey, D.W. Townsend, M.N. Maisey, *Positron Emission Tomography: Basic Science and Clinical Practice,* Springer, **3rd edition** (2003).

[36] Hamamatsu Corporation. *Photomultiplier Tubes (PMTs),* Hamamatsu. Web. **30 Apr** (2010), *http://sales.hamamatsu.com/en/products/electron-tubedivision/detectors/photomultiplier-tubes.php.*

[37] M. E. Phelps, *PET: Physics, Instrumentation, and Scanners,* Springer, (2006).

[38] J. Sæterstøl, *Characterization of Scintillation Crystals for Positron Emission Tomography,* Master dissertation, (2010).

[39] G. B. Saha, *Basic of PET imaging,* Physics, Chemistry and Regulations, second edition, (2005).

[40] M. N. Wernick, J. N. Aarsvold, *Emission Tomography: The fundamentals of PET and SPECT,* Elsevier academic press, (2004).

[41] How it works: Positron Emission, *http://courses.washington.edu/bioen508/Lecture5-B-PET.pdf.*

[42] M. Conti., *State of the art and challenges of time-of-flight PET,* Phys Med. **25** (2009) 1.

[43] S. Surti, S. Karp, L. Popescu, E. Daube-Witherspoon, M. Werner, *Investigation of time-of-flight benefit for fully 3-D PET,* IEEE Trans Med Imag. **25** (2006) 529.

[44] S. Surti, A. Kuhn, M.E. Werner, A.E. Perkins, J. Kolthammer, J.S. Karp, *Performance of Philips Gemini TF PET/CT Scanner with Special Consideration for Its Time-of-Flight Imaging Capabilities* J. Nucl Med. **48** (2007) 471.

[45] B. W. Jakoby, Y. Bercier, M. Conti, M. E. Casey, B. Bendriem, D. W. Townsend, *Physical and clinical performance of the mCT time-of-flight PET/CT scanner,* Phys Med Biol. **56(8)** (2011) 2375.

[46] V. Bettinardi, L. Presotto, E. Rapisarda, M. Picchio, L. Gianolli, M. C.Gilardi, *Physical performance of the new hybrid PET/CT Discovery-690,* Med Phys. **38(10)** (2011) 5394.

[47] N. G. Sharma, et al., *J-PET: A novel TOF-PET scanner using organic scintillators,* Journal of Chemical and Pharmaceutical Sciences ISSN:0974-2115 **4** (2016) 27.

[48] Sublima website, http://dev-sublima.keepwebsimple.de/objectives/performance.html, (2014).

[49] I. Vilardi..et al., *Optimization of the effective light attenuation length of YAP:Ce and LYSO:Ce crystals for a novel geometrical PET concept,* Nucl Instr & Meth **A564** (2006) 506.

[50] C. Casella, M. Heller, C. Joram, T. Schneider, *A high resolution TOF-PET concept with axial geometry and digital SiPM readout,* Nucl Instr & Meth **A736** (2014) 161.

[51] L. Jeffery et al., *High sensitivity, low cost PET using Lead-walled straw detectors,* Nucl Instr & Meth **A471** (2001) 88.

[52] N. Nader et al., *Novel lead-walled straw PET detectors for specialized imaging applications,* IEEE Nuclear Science Symposium Conference Record **4** (2005) 2895.

[53] G. Belli et al., *RPC: from High Energy Physics to Positron Emission Tomography,* Journal of Physics: Conference Series **41** (2006) 555.

[54] A. Blanco et al., *Efficiency of RPC detectors for whole-body human TOF-PET,* Nucl Instr & Meth **A602** (2009) 780.

[55] S. Niedźwiecki,..,N. G. Sharma, et al., *J-PET: A new technology for the whole-body PET imaging,* Acta Phys. Polon. B, **48** (2017) 1567.

[56] 3M Optical Systems, www.3M.com/Vikuiti

[57] E. Kubicz et al., *Beam profile investigation of the new collimator system for the J-PET detector,* Acta Phys. Polon. B **47** (2016) 549.

[58] J. L. Humm, A. Rosenfeld, A. Del Guerra, *From PET detectors to PET scanners* Eur. J. Nucl. Med. Mol. Imaging **3** (2003) 1574.

[59] P. Kowalski,..et al., *Scatter fraction of the J-PET tomograph,* Acta Phys. Polon. B **47** (2016) 549.

[60] O. Klein, Y. Nishima, Z. Phys. **52** (1929) 853.

[61] P. Moskal,..,N. G. Sharma, et al., *Test of a single module of the J-PET scanner based on plastic scintillators,* Nucl. Instr. and Meth., **A764** (2014) 317.

[62] M. Pałka,..,N. G. Sharma, et al., *Multichannel FPGA based MVT system for high precision time (20 ps RMS) and charge measurement scanners,* JINST **12** (2017) P08001 .

[63] P. Moskal, *A method and a system for determing parameters of reactions of gamma quanta within scintillation detectors of PET scanners,* Patent application:**PCT/EP2014/068355**, (2014).

[64] A. Strzelecki, *Image reconstruction and simulation of strip Positron Emission Tomography scanner using computational accelerators,* Ph.D dissertation (2016).

[65] National Electrical Manufactures Association et al. *Performance measurements of positron emission tomographs,* NEMA NU 2, (2012).

[66] J. Symrski,..,N. G. Sharma, et al., *Measurement of gamma quantum interaction point in plastic scintillator with WLS strips,* Nucl. Instr. and Meth., **A851**, (2017).